SF3B1 promotes tumor malignancy through splicing-independent activation of HIF1α

Patrik T. Simmler[1,6,#], Cédric Cortijo[1,#], Lisa M. Koch[2], Patricia Galliker[1], Moritz Schäfer[1], Silvia Angori[3], Hella A. Bolck[3], Christina Mueller[1], Ana Vukolic[1], Peter Mirtschink[1,+], Yann Christinat[1,°], Natalie R. Davidson[4], Kjong-Van Lehmann[4], Giovanni Pellegrini[5], Chantal Pauli[3], Daniela Lenggenhager[3], Ilaria Guccini[1], Till Ringel[1,6], Christian Hirt[1,6], Gunnar Rätsch[4], Matthias Peter[2], Holger Moch[3], Markus Stoffel[1] and Gerald Schwank[1,6*]

[1]Institute of Molecular Health Sciences, ETH Zurich, 8093 Zurich, Switzerland. [2]Institute of Biochemistry, ETH Zurich, 8093 Zurich, Switzerland. [3]Department of Pathology and Molecular Pathology, University Hospital Zurich, 8091 Zurich, Switzerland. [4]Department of Computer Science, ETH Zurich, 8093 Zurich, Switzerland. [5]Institute of Veterinarian Science, University of Zurich, 8057 Zurich, Switzerland. [6]Institute of Pharmacology and Toxicology, University of Zurich, 8057 Zurich, Switzerland.

[#]These authors contributed equally to this work.

*Correspondence: Gerald Schwank (schwank@pharma.uzh.ch)

[+]Present address: Institute of Clinical Chemistry and Laboratory Medicine, Department of Clinical Pathobiochemistry, University Hospital Dresden, 01307 Dresden, Germany. °Present address: Hôpitaux Universitaires de Genève, Service de Pathologie Clinique, Rue Michel-Servet 1, 1206 Genève, Switzerland.

SUMMARY

Mutations in the splicing factor SF3B1 are frequently occurring in various cancers and drive tumor progression through the activation of cryptic splice sites in multiple genes. Recent studies also demonstrate a positive correlation between expression levels of wildtype SF3B1 and tumor malignancy, but underlying mechanisms remain elusive. Here, we report that SF3B1 acts as an activator of HIF signaling through a splicing-independent mechanism. We demonstrate that SF3B1 forms a heterotrimer with HIF1α and HIF1β, facilitating binding of the HIF1 complex to hypoxia response elements (HREs) to activate target gene expression. We further validate the relevance of this mechanism for tumor progression. Monoallelic deletion of Sf3b1 impedes formation and progression of hypoxic pancreatic cancer via impaired HIF signaling, but is well tolerated in normoxic chromophobe renal cell carcinoma. Our work uncovers an essential role of SF3B1 in HIF1 signaling, providing a causal link between high SF3B1 expression and aggressiveness of solid tumors.

Keywords: hypoxia, glycolysis, HIF1 transcription, splicing, SF3B1, pancreatic cancer, chromophobe renal cell carcinoma

INTRODUCTION

SF3B1 is a core component of the U2 small nuclear ribonucleoprotein (snRNP) complex, involved in the recognition and selection of the branchpoint sequence in RNA splicing (Wahl et al., 2009). Missense mutations in this gene are frequently found in a number of different blood cancers (e. g. myelodysplastic syndrome, chronic lymphocytic leukemia) and solid tumors (e. g. breast and pancreatic cancers, uveal melanoma) (Quesada et al., 2012; Yoshida and Ogawa, 2014). They lead to aberrant 3' splice site usage, resulting in the creation of novel isoforms and/or nonsense mediated decay of hundreds of genes (Alsafadi et al., 2016; Darman et al., 2015; Kahles et al., 2018; Obeng et al., 2016a). For some of these genes missplicing was shown to promote tumor malignancy (i.e. *MAP3K7*, *PPP2R5A*) (Lieu et al., 2020; Liu et al., 2020; Obeng et al., 2016b), confirming the proto-oncogenic role of SF3B1. Interestingly, recent studies have also found a link between wildtype SF3B1 expression levels and tumor aggressiveness in pancreatic-, endometrial-, prostate-, liver- and breast cancer, with higher expression being associated with adverse prognosis (Alors-Perez et al., 2021; Jiménez-Vacas et al., 2019; López-Cánovas et al., 2021; Popli et al., 2020; Zhang et al., 2020). Considering that in the heart SF3B1 overexpression is induced by hypoxia (Mirtschink et al., 2015), and that solid cancers are often poorly oxygenated (Semenza, 2003), we hypothesized that upregulation of wildtype SF3B1 in tumors facilitates adaptation to hypoxia. In this study we demonstrate that SF3B1 physically interacts with hypoxia inducible factor (HIF)1α, and promotes transcriptional response to low oxygen by enabling HIF1α-HIF1β heterodimer binding to hypoxia response elements (HREs). We furthermore demonstrate the importance of this mechanism for the progression of cancers. While in pancreatic ductal adenocarcinoma (PDAC), one of the most hypoxic cancer types (Koong et al., 2000), *SF3B1* expression adversely correlates with patient survival in patients and experimental reduction of *SF3B1* levels in a mouse model severely comprises tumor development in a mouse model, in chromophobe renal cell carcinoma (chRCC), which generally grows in a normoxic environment, heterozygous loss of SF3B1 is well tolerated.

RESULTS

SF3B1 is a HIF target gene that positively regulates HIF pathway activity

We previously observed that SF3B1 is regulated by HIF in ischemic heart conditions (Mirtschink et al., 2015). To assess if *SF3B1* is also a HIF target gene in cancer, we first analyzed RNA sequencing (RNA-seq) data in four different solid cancers (PDAC, prostate cancer (PCA), hepatocellular carcinoma (HCC) and breast cancer (BRCA)). Supporting our assumption, we found a close correlation between the expression of *SF3B1* and the two

key components of HIF signaling, *HIF1A* and *ARNT* (*HIF1B*) in all four cancer types (Fig. 1A, B). In accordance with previous studies (Alors-Perez et al., 2021; Jiménez-Vacas et al., 2019; López-Cánovas et al., 2021; Popli et al., 2020; Zhang et al., 2020), we also observed a tendency for shorter survival in patients with higher *SF3B1* expression (Fig. 1C). Due to the well-known hypoxic environment found in PDAC (Koong et al., 2000), we then focused on this type of cancer to further investigate the role of SF3B1 in HIF signaling. In line with the hypothesis that *SF3B1* is a HIF target, we observed a strong correlation between the mean expression of 34 known HIF target genes and the expression of *SF3B*1 in human PDAC specimen (Spearman correlation coefficient = 0.52; Fig. 1D), and using a panel of patient-derived PDAC organoids and cell lines we detected a significant upregulation of SF3B1 expression upon experimental induction of hypoxia (Fig. 1E, Suppl. Fig. 1A and B). To assess if *SF3B1* is a direct target of HIF1α, we next expressed a constitutively active variant of HIF1α (HIF1α(ΔΔP)) in two cancer cell lines containing a *SF3B1*-promoter-luciferase in which the putative hypoxia-response elements (HRE) were mutated. Confirming direct regulation by HIF1α, only the wildtype *SF3B1*-promoter-luciferase reporter but not the mutant variant was activated (Fig. 1F, Suppl. Fig. 1C).

In a next step we determined whether *SF3B1* is merely a target gene or also a regulator of HIF1 signaling. We therefore manipulated *SF3B1* expression levels in multiple human PDAC cell lines and patient-derived PDAC organoids via overexpression, siRNA-mediated knock-down and monoallelic knockout (Suppl. Fig. 1D, E), and assessed its impact on HIF1 signaling. While *SF3B1* overexpression caused an increase of VEGF-luciferase reporter activity in a concentration-dependent manner (Fig. 1G, Suppl. Fig. 1F), and an upregulation of known HIF target genes (*BNIP3, CA9, EGLN3, GLUT1, VEGFA*) (Fig. 1H), reduction of *SF3B1* levels led to a significant downregulation of these target genes (Fig. 1H). In addition, the knock-down of *SF3B1* led to a 11.5-fold higher sensitivity to pharmacological inhibition of HIF1 (Suppl. Fig. 1G), and in Mia-Pa-Ca-2 cells, which are sensitive to hypoxia, overexpression of *SF3B1* increases proliferation rates in hypoxia but not in normoxia (Fig. 1I). Taken together, these data indicate that SF3B1 is not only a target gene but also a modulator of HIF1-signalling, facilitating adaptation of cancer cells to a hypoxic environment.

SF3B1 directly interacts with HIF1α

SF3B1 is a well-known splice factor, and it is therefore feasible that a decrease in SF3B1 levels leads to mis-splicing of HIF pathway components. However, upon siRNA-mediated knock-down of *SF3B1* we did not observe a reduction in protein levels of the two core components of HIF signaling, HIF1α and HIF1β (Fig. 2C and 3A), and while heterozygous loss of *SF3B1* in PANC-1 cells already led to a significant reduction in HIF response, the

71 50% decrease in *SF3B1* levels did not lead to defective splicing in a panel of genes prone to intron retention upon
72 *SF3B1* suppression (Paolella et al., 2017) (Suppl. Fig. 1H). Our results therefore indicate that SF3B1 may
73 modulate HIF signaling directly in a splicing-independent manner, prompting us to assess whether SF3B1
74 physically interacts with HIF1α or HIF1β. Immunoprecipitation assays indeed demonstrated that under hypoxic
75 conditions SF3B1 binds to the HIF1α/HIF1β transcriptional complex (Fig. 2A, B). While depletion of SF3B1 by
76 specific siRNAs did not compromise binding of HIF1β to HIF1α (Fig. 2C, Suppl. Fig. 1I), siRNA-mediated
77 depletion of HIF1α prevented co-immunoprecipitation of SF3B1 with HIF1β (Fig. 2D, Suppl. Fig. 1J). These data
78 suggest that SF3B1 binds the HIF1α-HIF1β heterodimer via HIF1α, but that this binding is not critical for HIF1α-
79 HIF1β heterodimer formation. To validate these findings, we produced recombinant SF3B1, HIF1α and HIF1β *in*
80 *vitro* in Sf9 insect cells and mixed the purified proteins prior to analyzing their interactions *in vitro*. In this setting,
81 SF3B1 co-immunoprecipitated with HIF1α and vice versa, irrespective whether HIF1β was present or not (Fig.
82 2E, F), but did not co-immunoprecipitate with HIF1β (Fig. 2F). Next, we aimed to identify the relevant domain
83 in HIF1α that mediates binding to SF3B1 by producing a series of deletion mutants of HA-tagged HIF1α and by
84 co-immunoprecipitating them with endogenous SF3B1 (Fig. 2G). Our results revealed that the bHLH-PAS-A-
85 PAS-B domain is necessary and sufficient for complex formation with SF3B1 (Fig. 2H).

86 Direct binding to the transcription factor HIF1α supports our assumption that SF3B1 modulates HIF signaling
87 independent from its role in the spliceosome complex. To further investigate this hypothesis, we
88 immunoprecipitated SF3B1 and HIF1α from hypoxic HEK293 cells, and immunoblotted for the presence of core
89 components of the U2 snRNAP complex. Indeed, only SF3B1, but not HIF1α, immunoprecipitated with the U2
90 components SF3B2, SF3B4 and SF3B14 (Fig. 2I). Confirming these findings, HA-tagged HIF1α in PANC-1 cells
91 co-immunoprecipitated with SF3B1, but not with SF3B2, SF3B4 and SF3B14 (Suppl. Fig. 1K).

92 Notably, we also assessed whether frequently occurring oncogenic mutations in SF3B1 could lead to enhanced
93 binding with HIF1α, thereby improving the ability of cancer cells to adapt to hypoxia. However, when HIF1α was
94 co-immunoprecipitated with oncogenic $SF3B1^{K700E}$, we observed slightly decreased binding compared to
95 wildtype SF3B1, and reduced HIF target gene expression under hypoxia (Suppl. Fig. 2 A-D). Furthermore, gene
96 expression analysis in patients with solid cancers showed a consistent trend for lower expression of HIF-target
97 genes in tumors containing $SF3B1^{K700E}$ (Suppl. Fig. 2E).

98 **DNA-binding of HIF1 to hypoxia response elements requires SF3B1**

99 Subcellular fractionation analysis revealed that siRNA-mediated knock-down of SF3B1 leads to reduced
100 chromatin-bound HIF1α, while leaving the total amount of HIF1α unaffected (Fig. 3A). This finding prompted us
101 to speculate that the interaction between HIF1α and SF3B1 is essential for the binding of the HIF1 complex to its
102 DNA target sites. Indeed, when we performed chromatin immunoprecipitations (ChIP) experiments we found that
103 SF3B1 is bound to HREs of various HIF target genes under hypoxic conditions (Suppl. Fig. 3A), and that this
104 binding is abolished upon knockdown of HIF1α (Suppl. Fig. 3B). Likewise, hypoxia-dependent binding of HIF1α
105 and HIF1β to HREs was strongly reduced on upon siRNA-mediated *SF3B1* depletion (Suppl. Fig. 3C – F). To
106 further assess SF3B1-dependency for HIF1 DNA binding in more depth, we performed HIF1α-ChIP-sequencing
107 on hypoxic PANC-1 cells treated with an SF3B1-targeting siRNA or a control siRNA. We identified 740 high-
108 confidence ChIP-seq peaks that were present in all three control replicates (Suppl. Table 1). Importantly, a major
109 fraction of these peaks was identified within close proximity (± 3kb) of genes that were transcriptionally
110 upregulated in hypoxia in PANC-1 cells under hypoxia (Fig. 3B), with 6 of the 10 most pronounced peaks being
111 located at the transcriptional start site of the well-known HIF1 targets ENO1, BNIP3L, PFKFB3, PGAM1, PGK1
112 and PDK1 (Suppl. Fig. 3G). In addition, *de novo* motif analysis in the regions ± 50 bp from the peak-summits
113 identified the previously-described RCGTG HRE-consensus sequence (Greenald et al., 2015) (Fig. 3C). In line
114 with our hypothesis that SF3B1 is required for HIF1α binding to its DNA target sites, we observed a strong
115 reduction in the HIF1α ChIP-seq peak-height upon *SF3B1* knock-down (Fig. 3D, E), with 99,73% of the 740
116 identified peaks being significantly reduced (FDR < 0.05, FC < -1.5) (Suppl. Fig. 3H, Suppl. Table 1). Differential
117 RNA-seq in PANC1 cells further enabled us to define a subset of direct HIF1α target genes (with HIF1α-ChIP-
118 peaks within a 3kb distance) that are dependent on SF3B1 for transcriptional upregulation upon hypoxia (Fig.
119 3F). As expected, unbiased pathway analysis revealed an enrichment of genes associated with HIF1 transcriptional
120 activity and glucose metabolism (Fig. 3G), demonstrating the importance of SF3B1 for metabolic adaptation to
121 hypoxia.

122 **Heterozygosity of *Sf3b1* restricts PDAC growth through impaired HIF-signalling**

123 To investigate the importance of SF3B1-mediated HIF regulation for PDAC, which is known for its hypoxic
124 environment and the necessity to upregulate glycolysis for tumor progression, we engineered a conditional *Sf3b1*
125 knockout mouse model where we reduced SF3B1 levels by heterozygous deletion of *Sf3b1* (Fig. 4A). The allele
126 was crossed into KPC (*LSL-Kras*$^{G12D/+}$*; LSL-Trp53*$^{R172H/+}$*; Ptf1a-Cre*) mice, where pancreas-specific activation of
127 oncogenic *Kras*^{G12D} and dysfunctional *Trp53* drives PDAC development within 9-14 weeks (Hingorani et al.,

128 2005). As expected, homozygous deletion of *Sf3b1* in the pancreas was not viable, and heterozygous deletion in
129 the KPC background (KPCS) led to a significant reduction in *Sf3b1* gene expression and protein levels (Fig. 4B,
130 Suppl. Fig. 4A, B). While no abnormalities with respect to anatomical appearance and weight of the pancreas
131 were observed in *Sf3b1*$^{+/-}$ mice in the non-cancerogenic *Ptf1a-Cre* background (Suppl. Fig. 4C, D), in the KPC
132 background heterozygous deletion of *Sf3b1* led to significant morphological differences (Suppl. Fig. 4E). At 7
133 weeks of age 60% of KPC mice but only 2% of the KPCS mice developed PanIN lesions (Suppl. Fig. 2F-I), and
134 at 13 weeks of age 100% of KPC mice developed PanIN lesions or PDAC whereas only 60% of KPCS mice had
135 grade 1 or 2 PanIN lesions (Fig. 4C, D; Suppl. Fig. 4G). Furthermore, KPC mice developed larger tumors (Suppl.
136 Fig. 4J, K), and were associated with considerably shorter survival (Fig. 4F).

137 While we hypothesized that heterozygous *Sf3b1* deletion inhibits PDAC progression via attenuating HIF activity,
138 impaired splicing could provide an alternative explanation. To discriminate between both scenarios, we
139 established 3D organoid cultures from KP- and KPS animals (Fig. 4G, Suppl. Fig. 5A). This enabled us to analyze
140 ductal tumor cells without stromal cell contamination (Boj et al., 2015), and to control the oxygen concentration
141 of the environment. We first confirmed that lentiviral transduction of a CRE recombinase induced expression of
142 KRAS^{G12D}, homozygous deletion of *p53*, and heterozygous deletion of *Sf3b1,* leading to a reduction in *Sf3b1*
143 mRNA and protein levels (Fig. 4H; Suppl. Fig 5B-D). We next analyzed global splicing efficiencies in KPC and
144 KPCS organoids under normoxic and hypoxic conditions, but did not find substantial differences in the percentage
145 of 'spliced-in' (PSI) events, including exon skips, alternative 3'and 5' sites, and intron retentions (Fig. 4I, J; Suppl.
146 Fig. 5E-L). In contrast, when we assessed the HIF pathway activity, we observed reduced expression of HIF target
147 genes upon heterozygous *Sf3b1* loss under hypoxia, but not under normoxia (Fig. 4K; Suppl. Fig. 5M). These
148 findings were confirmed *in vivo* by immunohistochemistry in mouse tumors, where the expression of HIF1α as
149 well as the HIF target GLUT1 was reduced in KPCS mice compared to KPC mice (Fig. 4L, M; Suppl. Fig. 5N-
150 Q), and in a functional assay for glycolysis. Incubation of organoids with radiolabeled [^{14}C]-2-Deoxy-D-glucose
151 showed no major differences in glucose uptake between KPC and KPCS organoids under normoxic conditions
152 (Suppl. Fig. 3R), but a decrease in glucose uptake in KPCS organoids under hypoxia (Fig. 4N). Supporting these
153 results, KPCS organoids grew significantly slower than KPC organoids in hypoxia but not in normoxia (Fig. 4O,
154 P). Together, our results demonstrate that heterozygous deletion of *Sf3b1* in PDAC does not lead to dysfunctional
155 splicing, but hampers adaptation to hypoxia, highlighting the importance of the SF3B1-HIF1α axis in pancreatic
156 cancer pathogenesis.

157 **Heterozygosity of *SF3B1* is tolerated in normoxic chromophobe renal cell carcinoma (chRCC)**

158 Gene expression analysis in TCGA datasets, as well as knock-down experiments in melanoma- and breast cancer
159 cell lines suggest that SF3B1-dependency for HIF target gene regulation is conserved across different solid
160 cancers (Fig. 1A, B; Suppl. Fig. 6A-D). However, our finding that wildtype SF3B1 levels are necessary for
161 mediating full adaptation to hypoxia suggests that frequent loss of heterozygosity in *SF3B1* should be tolerated
162 mainly in tumors with no or mild hypoxia, which do not rely on a metabolic shift to glycolysis. To test this
163 hypothesis, we focused on the analysis of chromophobe renal cell carcinoma (chRCC). This cancer shows an
164 exceptional high incidence for heterozygous loss of *SF3B1*-encoding chromosome 2 (Fig. 5A), which manifests
165 in lower *SF3B1* expression levels compared to the more frequent clear cell renal carcinoma (ccRCC) (Creighton
166 et al., 2013; Davis et al., 2014; Ohashi et al., 2019) (Suppl. Fig. 7A). To first confirm that *SF3B1* expression also
167 facilitates HIF signaling in chRCC, we established primary cell lines from chRCC biopsies and performed a
168 siRNA-mediated knockdown of *SF3B1*. Reduction in *SF3B1* levels indeed led to impaired transcriptional
169 response to hypoxia (Fig. 5B). After validating the high frequency of chromosome 2 loss in our cohort of chRCC
170 samples (Chr2 loss in Swiss-cohort in 60% of patients - Suppl. Fig. 7B, C), we performed IHC stainings to assess
171 HIF1α levels as a surrogate for HIF1 signaling activity. In line with our hypothesis, 90% of patient samples were
172 negative for HIF1α-staining, with the remaining 10% exhibiting low levels (Fig. 5C, D). In contrast, in samples
173 of clear cell renal cell carcinomas (ccRCC), a kidney cancer known for active HIF signaling(Creighton et al.,
174 2013), moderate or high HIF1α staining was observed in 48% of samples (Fig. 5C, D). Consistent with these
175 results, only 23% of ChRCC patients show moderate expression of the HIF target GLUT1 compared to 93% of
176 ccRCC patients (Fig. 5C, D), and genes involved in oxidative phosphorylation, but not glycolysis, were
177 upregulated in chRCC when compared to healthy tissue (Fig. 5E). These data support our hypothesis that loss of
178 heterozygosity of *SF3B1* is well-tolerated in chRCC, as this cancer does not rely on a metabolic shift to glycolysis.
179 Importantly, our data could also provide an explanation why only 4%-7% of patients of chRCC display tumor
180 metastasis(Davis et al., 2014), as for this process adaptation to low oxygen tension is pivotal (Ohta et al., 2011).
181 Indeed, when we stratified chRCC patients with loss of chromosome 2 into samples with low and high *SF3B1*
182 levels (Fig. 5F; Suppl. Fig. 7D), we observed a higher incidence of lymph node spreading (7% vs 43%) and poorer
183 prognosis in the group with upregulated *SF3B1* (Fig. 5G, H).

184

185 **DISCUSSION**

186 Our discovery of a splicing-independent role of SF3B1 in the HIF1 complex provides an unexpected mechanistical
187 explanation for recent studies, which correlated high SF3B1 levels with increased malignancy in solid tumors.
188 One difficulty in our study was to detangle the role of SF3B1 in HIF-signaling and splicing. However, the 50%
189 reduction of *SF3B1* levels resulting from loss of heterozygosity already led to a significant reduction in HIF-
190 signaling activity without impairing splicing, and overexpression of SF3B1 led to an increase in transcriptional
191 HIF response. In addition, while SF3B1 downregulation did not reduce HIF1 complex levels, it substantially
192 perturbed its ability to bind to HRE regions in HIF target genes.

193 HIF signaling plays an essential role in most solid cancers to adapt to low oxygen environments and to induce a
194 metabolic shift to anaerobic glycolysis. Its inhibition is therefore considered to be a highly promising treatment
195 approach (Muz et al., 2015; Semenza, 2003; Semenza, 2019). Most HIF inhibitors tested in clinical trials,
196 however, showed low specificity and interfered with other biological processes, leading to dose-limiting side-
197 effects (Semenza, 2019). Since binding of SF3B1 to HIF1α is direct, inhibition of this interaction could sensitize
198 tumor cells to low oxygen environments in a highly specific manner. Together with drugs blocking
199 heterodimerization of HIF1α/HIF1β, such compounds might therefore enable long-term treatment without the
200 occurrence of cross-resistance.

201 **ACKNOWLEDGMENTS**

202 Prof. Wilhelm Krek (W.K., Department of Biology, Institute of Molecular Health Sciences, ETH Zurich,
203 Switzerland), passed away in August 2018. He initiated this project and supervised the experiments until his
204 demise. This manuscript is dedicated to his memory.

205 We are grateful to D. Hanahan (EPFL, Lausanne, Switzerland) and T. Jacks (Koch Institute, MIT,
206 Cambridge/MA, USA) for providing mouse cancer cell lines and strains. We thank B. Luikart and W. Kaelin for
207 their plasmid constructs obtained via Addgene. This work was financed by grants from the Swiss National Science
208 Foundation, the Swiss Cancer League, the Walter Fischli Foundation, the University Research Priority Program
209 (URPP) in Translational Cancer Research (University of Zurich) and the Fritz Thyssen Foundation. Further
210 support was provided by the Tissue Biobank and the in-situ laboratory of the University Hospital Zurich, as well
211 as the Molecular Genetics Laboratory at the University Children's Hospital Zurich.

212 **AUTHOR CONTRIBUTIONS**

213 P.S., C.C., P.M., W.K. and G.S. conceived the study. P.S. and C.C. designed and executed most of the
214 experiments. G.S., W.K. and M.S. supervised the study. P.S. and G.S. wrote the manuscript with input from all
215 authors. L.M.K. performed the experiments related to mutant SF3B1. C.H., C.P and D.L established human cancer
216 organoid cultures. P.G. and C.M. performed isolation and cell biological characterization of murine organoids.
217 A.V. performed ultrasound imaging and was involved in the in-vivo study. T.R. was involved in the establishment
218 of CRISPR-mediated SF3B1 knockout cell lines. I.G. performed in vitro-experiments. P.S., K.V.L. and Y.C.
219 performed the *in-silico* analysis of HIF and SF3B1 expression in human cancers. N.R.D. analyzed RNA-splicing
220 in organoids. P.S. and M.S. performed ChIP-seq analysis. G.P. performed mouse tumor tissue IHC and quantified
221 tumor patterns. H.M., S.A. and H.A.B. performed chRCC tissue staining and evaluation and established chRCC
222 cell lines. H.M. was responsible for diagnosis and analysis of renal tumors.

223 **COMPETING INTERESTS**

224 The authors declare no competing interests.

225 **METHODS**

226 **TCGA data analysis**

227 TCGA RNA-seq expression and clinical data were downloaded either from the TCGA website (https://tcga-
228 data.nci.nih.gov), from The Human Protein Atlas (Uhlen et al., 2017) (https://proteinatlas.org) or from The cBio
229 Cancer Genomics Portal (Cerami et al., 2017; Gao et al., 2014) (https://cbioportal.org). For survival analysis,
230 patients were stratified by the median of *SF3B1* gene expression, except for the chRCC analysis. There, the upper
231 quartile of *SF3B1* expression in patients with chromosome 2 loss was used for stratification. In the survival
232 analysis of chRCC patients, a missing variable (months) of one deceased patient in the *Chr2 loss, SF3B1 high*
233 cohort was imputed by using the mean value of all deceased patients in the unstratified dataset. The hypoxia
234 signature was computed as the average expression of 34 hypoxia-inducible genes represented by *CA9,*
235 *NDUFA4L2, EGLN3, NDRG1, PFKFB4, ADM, NRN1, CA12, ENO2, ZNF395, RAB20, DDIT4, SLC7A5, BNIP3,*
236 *HMOX1, POU5F1, ALDOC, PDK1, LDHA, SLC2A1, BNIP3L, STC2, HK2, CP, LOX, MUC1, VEGFA, SLC16A3,*
237 *MXI1, GYS1, COL5A1, PPP1R3C, TXNIP, LRP1*. K700E mutations are based on a uniform recalled variant
238 dataset. RNA-seq data has been uniformly re-aligned across all 8255 cancer patient samples. Only non-alternate
239 axons are used for gene expression quantification that has been quantile normalised (Kahles et al., 2018). Data
240 has been made available here: https://gdc.cancer.gov/about-data/publications/PanCanAtlas-Splicing-2018.

241 **Cell culture**

242 SK-MEL-28, PANC-1, MDA-MB-231, Mia-PaCa-2 and HEK293T cells were maintained in Dulbecco's modified
243 Eagle's medium (DMEM, Invitrogen) supplemented with 10% FBS, and 4 mM L-glutamine. AsPC-1 and BxPC-
244 3 cells were maintained in Roswell Park Memorial Institute (RPMI, Invitrogen) supplemented with 10% FBS and
245 4 mM L-glutamine. Cell lines were cultured at 37 °C in 5% CO_2. Sf9 insect cells were grown in suspension at
246 27°C in Sf-900 II SFM medium (Invitrogen) supplemented with penicillin/streptomycin (Sigma-Aldrich). Cell
247 density was monitored regularly and was maintained between 0.5 and 2 x10^6 cells/ml. All cell lines have been
248 authenticated by Microsynth and regular mycoplasma tests were performed using the ScienCell Mycoplasma PCR
249 detection kit (Cat. No. 8208).

250 **Quantitative real-time PCR analysis**

251 RNA was isolated using the nucleospin RNA kit (Macherey-Nagel) and reverse-transcribed to cDNA (kit: Applied
252 Biosystems, ref. 43698813). SYBR-green based quantitative real-time PCR (qRT–PCR) was performed on a

253 LightCycler 480 (Roche). C_t values were normalized to the housekeeping gene *TBP* for human samples and to
254 *Actb* or *Ccny* for the mouse samples. Primer sequences are listed in Supplementary Table 3.

255 **Luciferase assays**

256 Cells were co-transfected with a *Vegf*-HRE-luciferase reporter plasmid, or a *Sf3b1*-HRE-luciferase reporter
257 plasmid together with different plasmids using lipofectamine 2000 (Invitrogen). A renilla luciferase plasmid was
258 co-transfected for internal control. Cells were collected 24 hrs after transfection, and luciferase activity analyzed
259 on a TECAN M1000 PRO using the dual-luciferase reporter assay system (Promega E1980). The assays were
260 carried out according to the manufacturer's instructions.

261 **Transient transfections**

262 siRNAs were transfected using Lipofectamine-RNAiMax reagent (Invitrogen). We used Qiagen human
263 si*SF3B1*#1 (SI04159456), human si*SF3B1*#2 (SI04161766) and human si*HIF1A 5'*-CUG AUG ACC AGC AAC
264 UUG A-3' and 5'-UCA AGU UGC UGG UCA UCA G-3'. For transient overexpression studies, DNA plasmids
265 were transfected with Lipofectamine 2000 (Invitrogen) according to the manufacturer's protocol.

266 **Lentivirus production and transduction**

267 Lentiviral particles were produced in HEK-293T cells. HEK-293T cells were purchased from American Type
268 Culture Collection (ATCC). Cells were transduced with lentivirus by adding virus-containing supernatants to the
269 cell culture medium.

270 **Chromatin immunoprecipitations (ChIP)**

271 ChIP assays were performed using the ChIP-IT Kit (Active Motif) according to the manufacturer's instructions.
272 ChIP was performed with HIF1α antibody from Abcam (ab2185), SF3B1 antibody from MBL International
273 (D221-3), an HIF1β antibody from Novus Biological (NB 100-124), or an anti-IgG antibody from Abcam
274 (ab171870). Primer sequences used are listed in Supplementary Table 3.

275 **ChIP-sequencing: Sample preparation**

276 HIF1α-ChIP-assays for ChIP-seq was performed using the SimpleChIP® Enzymatic Chromatin IP Kit (#9003)
277 from Cell Signalling Technologies according to the manufacturer's instructions. In brief, cells from 4 15-cm
278 dishes were cross-linked using formaldehyde for 5 minutes under hypoxia, the cross-linking was subsequently

279 quenched with incubation of with 125 mM glycine (final concentration) for 5 minutes at normoxia and the cells
280 were collected. Cells were lysed and nuclei were isolated by centrifugation. DNA was fragmented by micrococcal
281 nuclease digestion for 20 minutes at 37°C, and nuclei were disrupted by brief sonication 10 minutes on a high
282 setting. Cleared extracts were subjected for immunoprecipitation using HIF1α (D1S7W XP® Rabbit mAb
283 #36169) and IgG antibodies as control. After reversal of the cross-link, DNA was isolated and its concentration
284 measured with Qubit dsDNA HS assay kit (Q32851) according to the manufacturers instruction. For controlling
285 potential amplification-biases during library-preparation, 0.2 ng of drosophila chromatin, treated as described
286 above for the experimental samples, was spiked-in for every sample before library-preparation.

287 **ChIP-sequencing: Library-preparation and sequencing**

288 The NEBNext® Ultra™ II DNA Library Prep Kit from NEB (New England Biolabs, Ipswich, MA) in the
289 succeeding steps. ChIP samples (1 ng) were end-repaired and adenylated. Adapters containing the index for
290 multiplexing were ligated to the fragmented DNA samples. Fragments containing adapters on both ends were
291 enriched by PCR. The quality and quantity of the enriched libraries were measured using Qubit® (1.0)
292 Fluorometer and the Tapestation (Agilent, Waldbronn, Germany). The product is a smear with an average
293 fragment size of approximately 300 bp. The libraries were normalized to 10nM in Tris-Cl 10 mM, pH8.5 with
294 0.1% Tween 20. The libraries were sequenced single read 100 bp using the Illumina Novaseq 6000 (Illumina, Inc,
295 California, USA). Reads were quality-checked with fastqc which computes various quality metrics for the raw
296 reads.

297 **ChIP-sequencing: Computational analysis**

298 SnakePipes "ChIP-seq" pipeline (Bhardwaj et al., 2019) was used for the analysis of the sequencing data according
299 to the developer's guidelines. In brief, reads were trimmed, deduplicated and aligned simultaneously to the
300 masked genomes of homo sapiens (GRCh38.p13) and drosophila melanogaster (BDGP6.32) published by
301 Ensembl. Three replicates for each condition were used. On average, 86 million (SD: 18 million) reads per sample
302 were uniquely mapped to the hybrid genome. Peaks were identified by MACS2(Zhang et al., 2008), using merged
303 reads of two chromatin inputs per condition for background normalization. CSAW (Lun and Smyth, 2015) was
304 applied for differential binding analysis, whereby size factors were calculated by computing the relative number
305 of mapped reads to the drosophila genome for each sample. Genes in proximity of peaks were identified by
306 searching for nearest transcripts. For subsequent analyses, only peaks that were identified in all of the 3 siCtrl-
307 ChIP replicates were considered (high-confidence peaks). Motif recognition was performed with MEME (Bailey

308 and Elkan, 1994), using sequences of -49 and +50 bp of the summit of the respective peak. A maximum of 1000
309 input sequences was considered for the motif-recognition. The following parameters were used: *-dna -mod zoops*
310 *-objfun cd -revcomp -minw 10 -maxw 15*. The heatmap of high-confidence peaks was computed with
311 deeptools/compute matrix and /plotheatmap. Exemplary peaks were visualized using pyGenomeTracks on two
312 corresponding replicates with comparable sizefactors (0.93 / 0.91) to facilitate visual comparison. Pathway
313 analysis on the gene-set described in Fig. 3F & G was performed with Enrichr on the BioPlanet database.

314 **Subcellular protein fractionation**

315 Subcellular protein fractionation and isolation of chromatin fractions was performed using the Subcellular Protein
316 Fractionation Kit for Cultured Cells kit from Thermo Fisher, following the instructions of the manufacturer.
317 Soluble nuclear and chromatin-bound nuclear extracts were loaded on an SDS–PAGE gel and subjected to western
318 blotting.

319 **Immunoblotting and antibodies**

320 Protein lysates were resolved on polyacrylamide minigels and transferred onto nitrocellulose membrane by semi-
321 dry transfer. The following antibodies were used for immunoblotting: rabbit HIF1α (catalogue no. NB-100-479;
322 Novus Biologicals), mouse SF3B1 (catalogue no. D221-3; MBL International), mouse HIF1α (catalogue no. NB
323 100-124; Novus Biologicals), mouse SF3B2 (catalogue no. ab56800; Abcam), rabbit SF3B4 (catalogue no.
324 ab157117; Abcam), rabbit SF3B14 (catalogue no. NBP1-87431; Novus Biologicals), rabbit α-tubulin (catalogue
325 no. ab18251; Abcam), rabbit CA9 (catalogue no. NB-100-417; Novus), rabbit PKM2 (catalogue no. 3198; Cell
326 Signaling), rabbit PDK1 (catalogue no. 3061S; Cell Signaling), mouse HA-tag (catalogue no. 26183; Thermo
327 Scientific), rabbit p53 (catalogue no. FL-393; Santa Cruz), mouse KrasG12D (catalogue no. 26036; Neweastbio),
328 mouse total-Ras (catalogue no. 3965; Cell Signaling), rabbit p-Mek (catalogue no. 9154; Cell Signaling), rabbit
329 total-Mek (catalogue no. 9122S; Cell Signaling), rabbit p21 (catalogue no. ab109199; Abcam), rabbit p16
330 (catalogue no. ab51243; Abcam). Immunodetection and visualization of signals by chemiluminescence was
331 carried out by using the ImageQuant LAS 4000 mini (GE Healthcare). For immunoprecipitation, transfected cells
332 were lysed in cell lysis buffer TNN (50 mM Tris-HCl pH 7.5, 250 mM NaCl, 5 mM EDTA, 0.5% NP-40,
333 50 mM NaF, 1 mMDTT, 1 mM PMSF, and protease inhibitor cocktail) for 30 min. Magnetic dynabeads
334 (Invitrogen) were incubated first with the primary antibody for 10 min at room temperature, washed and then
335 incubated with the cell lysate for 3 hours at 4°C. The assays were carried out according to the manufacturer's
336 instructions. Finally, the beads were boiled in 2x sample buffer for 5 min and eluents were analyzed by Western

337 blotting. For co-immunoprecipitation with recombinant proteins, magnetic dynabeads (Invitrogen) were incubated
338 first with the primary antibody and then incubated with the recombinant proteins for 2 hours at 4°C.

339 **Human PDAC organoid culture**

340 Human PDAC organoids were established from patients' surgical specimens and cultured as described in full
341 detail by (Hirt *et al*, manuscript under revision). Human pancreatic tissue samples were provided by the
342 Department of Pathology and Molecular Pathology, University Hospital Zurich, based on informed consent and
343 study approval from the ethical committee (BASEC-Nr. 2017-01319). For all samples, the diagnosis of PDAC
344 was confirmed on corresponding tissue slides reviewed by board-certified pathologists. To establish organoid
345 lines, tissue was chopped and digested in full medium containing collagenase type II (5 mg/ml). The digestion
346 was stopped with advanced DMEM/F12 medium supplemented with HEPES (10mM), Glutamax (1%) and
347 penicillin/streptomycin (1%). Cells were seeded as 20µl drops of Matrigel (Corning, growth factor reduced) into
348 a 48-well suspension culture plate. Human PDAC organoids were cultured in Advanced DMEM supplemented
349 with 10×10^{-3} M HEPES, 1x Glutamax, 1% Penicillin/Streptomycin, 1x B27, 1.25×10^{-3} M N-acetylcysteine,
350 50% Wnt3a conditioned medium (CM), 10% R-spondin-1 CM, 10% noggin CM, 10×10^{-3} M nicotinamide, 1 ×
351 10−6 M prostaglandin E2, 50 ng mL^{-1}, EGF, 10×10^{-9} M gastrin, 100 ng mL^{-1} FGF10 and 0.5×10^{-6} M A83-01.

352 **RCC ethics statement and patient selection**

353 All tissue samples were made available by the Tissue Biobank of the Department of Pathology and Molecular
354 Pathology, University Hospital of Zurich, Switzerland and collected as described previously (Bolck et al., 2019).
355 The local ethics commission approved this study (BASEC_2019-01959) and patients gave written consent. The
356 retrospective use of normal and tumor tissues of RCC patients is in accordance with the Swiss Human Research
357 Act, which allows the use of biomaterial and patient data for research purposes without informed consent under
358 certain conditions that include the present cases (article 34). All tumors were reviewed by a board-certified
359 pathologist and histologically classified according to the World Health Organization guidelines.

360 **ChRCC tissue processing and generation of cell models**

361 Renal tumors were surgically resected and underwent routine tissue processing and rapid sectioning for diagnostic
362 purposes and generation of cell models (including formalin fixation and paraffin embedding, snap freezing of
363 fresh tumor and normal tissue). Fresh tissue samples macroscopically identified as cancer by a pathologist with
364 specialization in uropathology (H. Moch) were placed into sterile 50-ml conical tubes containing transport media

365 (RPMI (Gibco, Waltham, MA) with 10 % fetal calf serum (FCS, Gibco) and Antibiotic-Antimycotic® (Gibco))
366 and stored at 4 °C until further processing. Briefly, samples were rinsed with PBS and subsequently cells were
367 isolated by finely cutting the tissue into small pieces followed by collagenase A digestion for 1-3 hours at 37 °C.
368 The slurry was passed through a 100 µm cell strainer to remove large fragments and the Collagenase A digestion
369 was quenched with DMEM containing 10-20 % FCS. Cells were washed once with PBS and if necessary,
370 erythrocytes were lysed. Finally, cell viability was evaluated by trypan blue dye exclusion and an appropriate
371 number of cells was resuspended in Renal Epithelial Cell Growth Medium 2 (Promocell). This suspension was
372 seeded into collagen I-coated cell culture dishes (Corning, Corning, NY) containing 30–50 % confluent
373 Mitomycin C-treated mouse embryonic fibroblasts CF6 (ThermoFisher). Subsequently, the co-culture was
374 maintained in Renal Epithelial Cell Growth Medium 2 in a humidified incubator at 37 °C with 5% CO_2. The
375 medium was replaced earliest 5 days after initial plating and subsequently every three to four days. Cells were
376 expanded by passaging without the addition of new CF6 feeder cells in subsequent passages.

377 **RCC immunohistochemistry**

378 For immunohistochemical (IHC) analyses, a tissue microarray (TMA) and whole tissue sections of primary RCCs
379 from the Department of Pathology and Molecular Pathology, University Hospital of Zurich, Switzerland were
380 used (Dahinden et al., 2010). Clinicopathological parameters of the RCC specimens are described in
381 Supplementary Table 4. Formalin-fixed paraffin-embedded (FFPE) cell pellets from cell cultures were prepared
382 as previously described (Struckmann et al., 2008). For histological evaluation, FFPE specimens were sectioned
383 (2 µm) and stained with hematoxylin and eosin (HE). For IHC, 2 µm sections were transferred to glass slides
384 followed by antigen retrieval. Antibodies used for IHC are summarized in the table below. IHC was performed
385 using the Ventana Benchmark automated system (Roche, Ventana Medical Systems, Oro Valley, AZ) and
386 Ventana reagents. The Optiview DAB IHC detection and the Discovery Chromomap DAB Kits (Roche, Ventana
387 Medical Systems) were used to stain with the antibodies against Glut1 and SF3B1, respectively. The staining
388 procedure for HIF1α was carried out with the automated Leica BOND system using the Bond Polymer Refine
389 Detection Kit (Leica Biosystems, Wetzlar, Germany).

Antibody	Name/Clone	Dilution IHC	Supplier
SF3B1	EPR11986	1:100	Abcam
HIF1α	HIF-1 alpha antibody [mgc3]	1:400	Abcam
GLUT1	Glucose Transporter type 1	1:1000	Millipore

390

391 **RNA-extraction of chRCC patient samples**

392 RNA extraction from FFPE specimens of chRCC was performed using the Maxwell® 16 Tissue DNA Purification
393 Kit (Promega). RNA quality was assessed with the RNA Qubit™ RNA HS Assay Kit (ThermoFisher).
394 Subsequently, cDNA was prepared using the Superscript IV Vilo Mastermix (Thermo Fisher).
395
396 **SF3B1 quantification in chRCC patient samples**
397 The quantitative measurements of SF3B1 were performed using the Taqman Fast Advanced master mix (Thermo
398 Fisher) with 5 ng/µL ng of cDNA in each technical duplicate and the cycling parameters according to the protocol
399 on a ViiA7 (Thermo Fisher). Primer and probe set assay IDs for the TaqMan assays were Hs00961640_g1 for
400 SF3B1 and Hs03929097 for GAPDH, (ThermoFisher). Normal tissue was used to normalize the quantitative
401 analysis of all samples. For the other genes assessed, regular qPCR was performed as described above.
402
403 **Analysis of Copy Number Variations (CNVs)**
404 DNA was processed and hybridized to Affymetrix CytoScan HD array according to manufacturer's protocol.
405 Sample level quality control was initially assessed by Affymetric ChAS software, version 2.0 and probeset.txt
406 files were exported. These served as input for the *rCGH* R package (v. 3.8) obtained from Bioconductor. The
407 comprehensive comparative genomic hybridization (CGH) analysis workflow provided by *rCGH* was used for
408 log2 relative ratio (LRR) calculation (the sample DNA signals against a normal two-copy DNA reference), profile
409 centralization and profile segmentation. Significant focal copy number alterations were identified from segmented
410 data using GISTIC 2.05. Subsequently, absolute copy numbers were inferred.
411
412 **Plasmid design**

413 Deletion mutants of HIF1α were generated by PCR using a pcDNA3-HA-HIF1α plasmid (addgene 18949) as
414 template. We designed specific primers that border the domain to be deleted on both sides in order to remove the
415 different targeted domains of HIF1α.

416 **Baculovirus expression system**

417 Baculovirus expression vectors expressing Strep-Tag II epitope tagged-SF3B1, HIF1α, or HIF1β were constructed
418 by inserting the cDNA of corresponding genes into a pFBDM plasmid. Strep-Tag II tagged-SF3B1, HIF1α, or
419 HIF1β were expressed in Sf9 cells that had been infected with recombinant baculovirus as described in the Bac-
420 to-Bac® Baculovirus Expression System from Invitrogen.

421 **Immunoprecipitation and Co-immunoprecipitation (CoIP) assays**

422 For immunoprecipitation, transfected cells were lysed in cell lysis buffer TNN (50 mM Tris-HCl pH 7.5,
423 250 mM NaCl, 5 mM EDTA, 0.5% NP-40, 50 mM NaF, 1 mM DTT, 1 mM PMSF, protease inhibitor cocktail
424 and Pierce™ Universal Nuclease for Cell Lysis) for 30 min. Magnetic dynabeads (Invitrogen) were incubated
425 first with the primary antibody for 10 min at room temperature, washed and then incubated with the cell lysate
426 for 3 hours at 4°C. The assays were carried out according to the manufacturer's instructions. Finally, the beads
427 were boiled in 2x sample buffer for 5 min and eluents were analyzed by Western blotting.
428 For co-immunoprecipitations with transiently overexpressed flag-Sf3b1 and flag-Sf3b1^{K700E}, transfected
429 HEK293T cells were lysed in TNN buffer as described above. Lysates were cleared by centrifugation at 16 000 x
430 g for 30 minutes. Anti-FLAG® M2 Magnetic Beads (Merck) were equilibrated in lysis buffer and incubated with
431 the cell lysate for 1 hours at 4°C. The beads were washed at least 4 times with TNN buffer and boiled in 2x sample
432 buffer for 5 min. The eluents were analyzed by western blotting.
433 For co-immunoprecipitation with recombinant proteins, magnetic dynabeads (Invitrogen) were incubated first
434 with the primary antibody and then incubated with the recombinant proteins for 2 hours at 4°C.

435 **Mouse strains**

436 *LSL-Kras$^{G12D/+}$; LSL-Trp53^{R172H}* (KP), and *LSL-Kras$^{G12D/+}$; LSL-Trp53$^{R172H/+}$; Ptf1a-Cre* (KPC) were obtained
437 from Tyler Jack's (Howard Hughes Medical Institute). Sf3b1 flox/flox mice were generated by targeting exon
438 five and six of the Sf3b1 gene. These exons were floxed with LoxP sites and the targeted region was about 3.0
439 kb. A LoxP/FRT-flanked neomycin resistance cassette was placed 277 bp upstream of exon five and six for
440 selection. Chimeric mice were generated via electroporation in embryonic stem cells followed by microinjection
441 in blastocysts and implantation into foster mice. For all *in vivo* experiments, except the survival experiment, mice
442 between the age of 7 and 13 weeks were used. Female and male mice were used for all experiments. All mice
443 were maintained in a SPF animal facility at the ETH Phenomics Center EPIC at ETH Zürich. Maintenance and
444 animal experiments were conducted in accordance with the Swiss Federal Veterinary Office (BVET) guidelines.
445 Animal surgeries and ultrasound (Vevo 2100 system) analysis was performed blinded by a veterinarian. Animal
446 numbers for experiments were chosen based on expected mortality rates and phenotypical changes of the pancreas
447 in mice.

448 **Histological and immunohistochemical analysis (murine specimen)**

449 Following euthanasia, pancreata were removed, weighed and fixed overnight in 10% neutral buffered formalin
450 (Formafix Switzerland AG, Hittnau, Switzerland). The tissue was embedded in paraffin and cut serially into 3-5-
451 µm sections, which were stained with hematoxylin and eosin (HE) and Masson trichrome for the assessment of
452 fibrosis. Histological analysis, including murine pancreatic intraepithelial neoplasia (mPanIN) grading and
453 assessment of the proportion of affected versus unremarkable pancreatic parenchyma, was carried out in the HE-
454 stained sections in a blinded fashion by an ECVP-board certified veterinary pathologist (GP), according to
455 previously reported criteria(Hruban et al., 2006). Immunohistochemistry (IHC) was conducted on consecutive
456 paraffin-embedded sections using the primary antibodies against HIF1α (rabbit polyclonal, Novus Biological,
457 NB100-479, 1:500), SF3B1 (rabbit monoclonal, clone number EPR11986, Abcam, ab172634, 1:100), GLUT-1
458 (rabbit polyclonal, Merck Millipore, #400060, 1:100), Ki-67 (rabbit monoclonal, clone name 30-9, Ventana
459 Roche, 790-4286, 1:400), cleaved caspase 3 (rabbit monoclonal, clone number D3E9, Cell Signaling, Cell
460 Signaling, #9579, 1:400) and CD31 (rabbit polyclonal, Santa Cruz, sc-1506R, 1:1000). All immunostains were
461 performed in Ventana Discovery (Ki-67 and cleaved caspase 3) or Dako autostainers using 3,3' diaminobenzidine
462 (DAB) chromogen (Dako-Agilent Technologies, Denmark). All slides were scanned using digital slide scanner
463 NanoZoomer-XR C12000 (Hamamatsu, Japan) and images were taken using NDP.view2 viewing software
464 (Hamamatsu). mPanIN were counted manually in 10 high power fields (HPF) in each HE-stained section.
465 Automated quantitative analysis was carried out on the digital slides using the Visiopharm Integrator System
466 (VIS, version 4.5.1.324, Visiopharm, Hørsholm, Denmark). Briefly, a linear threshold classification allowed
467 recognition of the blue (Masson trichrome) or DAB brown (IHC) structures in 20 regions of interest (ROI) sized
468 0.237 mm^2 (the area of an HPF with one ocular of 22 mm field of view), randomly selected across the pancreatic
469 parenchyma. Results were expressed as percentage of positive area/ROI vs total parenchyma/ROI (Masson
470 trichrome, HIF-1α, GLUT1, CD31) or average number of positive nuclei or cells/ROI (SF3B1, Ki-67, cleaved
471 caspase 3).

472 **Heterozygous knockout of SF3B1 by CRISPR-Cas9**

473 We used the sgRNA-Designer platform by the Broad Institute to design sgRNAs for targeted gene knock-out
474 (https://portals.broadinstitute.org/gpp/public/analysis-tools/sgRNA-design). Two distinct sgRNAs were used:
475 sgSF3B1_A (5'-TAATCTTCATCAATCAATAG-3') and sgSF3B1_B (5'-AAGATCGCCAAGACTCACGA-
476 3'). According to the protocol from Shalem et al., we adapted the sgRNA design for subsequent cloning into the
477 LentiCRISPRv2 backbone (Shalem et al., 2014). Cells were transduced with lentivirus and selected with
478 puromycin. Heterozygous knock-out of the target gene was validated with deep sequencing for PANC-1 and

479 AsPC-1 cells at two distinct time-points, to assess the enrichment of in-frame indels. Primers were designed
480 flanking the predicted sgRNA cut-site and containing primer binding sites for Illumina TruSeq Deep sequencing
481 primers. After purification, the amplicons were sequenced on an Illumina MiSeq System, with a minimum of
482 5'000 reads. Analysis of editing events was performed with CRISPResso V1.0.1.

483 **Murine pancreatic ductal organoid culture**

484 Pancreatic ducts were isolated from the whole organ of 13 weeks old KP and KPS mice as previously described
485 (Huch et al., 2013). Each organoid line was isolated from an individual mouse. Isolated ducts as well as the
486 ensuing organoids were embedded in growth-factor reduced (GFR)-Matrigel (Corning), and cultured in organoid
487 medium (OM), which is composed of AdDMEM/F12 (Gibco) supplemented with GlutaMAX (Gibco), HEPES
488 (Gibco), Penicillin-Streptomycin (Invitrogen), B27 (Gibco), N-2 (Gibco), 1.25 mM N-Acetyl-L-cysteine (Sigma),
489 10 nM Gastrin I (Sigma) and the growth factors: 100 ng/ml FGF10 (Peprotech), 50 ng/ml EGF (Peprotech), 100
490 ng/ml Noggin, 100 ng/ml RSPO-1 (Peprotech), and 10 mM Nicotinamide (Sigma). For the first week after duct
491 isolation the culture medium was supplemented with 100 µg/ml Primocin (InvivoGen).

492 **Lentiviral production and transduction of organoids**

493 The plasmids FUG-T2A-GFP-Cre and control GFP were purchased from Addgene #66691 and lentiviral particles
494 were produced in HEK-293T cells using X-tremeGene 9 DNA Transfection Reagent (Roche). Upon
495 ultracentrifugation concentrated virus particles were stored at -80°C and used to infect pancreatic ductal organoid
496 cultures as previously described (Huch et al., 2013). Briefly, upon dissociation of the GFR-Matrigel, organoid
497 cultures were broken down into single cells using TrypLE Express (Gibco) and fire-polished glass Pasteur
498 pipettes. Single cells were transferred to maximum recovery microtubes (Axygen) and centrifuged at 800 g for 5
499 min at 4°C. The pellets were resuspended in 250 µl OM and inoculated with 10 µl of concentrated virus particles
500 that was then incubated at 37°C for 4-6 h. After a washing step, the cells were seeded in GFR-Matrigel and grown
501 in OM. Two to three weeks later the pool of GFP-expressing organoids was dissociated again into single cells and
502 subjected to FACS analysis (MoFlo® Astrios™ EQ) to sort for GFP-positive cells. The cells were put back into
503 culture and used for subsequent experiments.

504 **Organoid proliferation assay**

505 Organoids were seeded as single cells at a density of 500 cells/µl GFR-Matrigel (Corning). 48 hours after seeding,
506 cells were exposed to 1% O_2 in a hypoxia chamber (SCI-tive Hypoxia Workstation, Baker Ruskinn) or kept in a

507 cell culture incubator at 21% O_2. At depicted time-points, the organoids were recovered from the matrigel and
508 dissolved in 200 µl TE-buffer. After 3 freeze-thaw cycles, the amount of DNA was quantified with Quant-iT™
509 PicoGreen™ dsDNA Assay Kit (ThermoFisher Scientific) according to the manufacturer's instructions. Absolute
510 values were normalized to the DNA-content 48 hours after seeding.

511 **[^{14}C] 2-Deoxy-D-glucose uptake**

512 For organoid experiments, 3 wells of 50 µl matrigel-embedded organoids per condition were seeded in a 24-well
513 plate. On day 3, cells were kept in normoxia or exposed to hypoxia (at 1% O_2) for 12 hours. The medium was
514 replaced with DMEM containing uniformly-labelled [^{14}C] 2-Deoxy-D-glucose (Hartmann Analytic) at a
515 concentration of 150 µci/mmol and 5 mM glucose. Cells were washed twice with PBS just before harvesting.
516 Radioactivity counts were normalized to cell number.

517 **Illumina RNA sequencing experiment**

518 Multiple organoid lines (5x KPC, 4x KPCS) were seeded as described, where each line was derived from an
519 individual mouse. After 48 hours of exposure to 1% O_2 or 21% O_2, organoids were harvested and RNA was
520 extracted using the NucleoSpin® RNA kit (Macherey-Nagel) according to the manufacturer's instructions. For
521 each organoid line, 2-3 wells of organoids from a 24 well plate were harvested in lysis buffer RA1 (RNA
522 extraction kit, MN) supplemented with TCEP (Tris(2-carboxyethyl)phosphine hydrochloride). For library
523 preparation, the quantity and quality of the isolated RNA was determined with a Qubit® (1.0) Fluorometer (Life
524 Technologies, California, USA) and a Bioanalyzer 2100 (Agilent, Waldbronn, Germany). The TruSeq Stranded
525 mRNA Sample Prep Kit (Illumina, Inc, California, USA) was used in the succeeding steps. Briefly, total RNA
526 samples (1 µg) were ribosome depleted and then reverse-transcribed into double-stranded cDNA with
527 Actinomycin added during first-strand synthesis. The cDNA samples were fragmented, end-repaired and
528 polyadenylated before ligation of TruSeq adapters. The adapters contain the index for multiplexing. Fragments
529 containing TruSeq adapters on both ends were selectively enriched with PCR. The quality and quantity of the
530 enriched libraries were validated using Qubit® (1.0) Fluorometer and the Bioanalyzer 2100 (Agilent, Waldbronn,
531 Germany). The product is a smear with an average fragment size of approximately 360 bp. The libraries were
532 normalized to 10nM in Tris-Cl 10 mM, pH8.5 with 0.1% Tween 20. Cluster generation and sequencing involved
533 application of the TruSeq SR Cluster Kit v4-cBot-HS or TruSeq PE Cluster Kit v4-cBot-HS (Illumina, Inc,
534 California, USA) using 8 pM of pooled normalized libraries on the cBOT. Sequencing were performed on the

535 Illumina HiSeq 4000 paired end at 2x 100 bp (2x at least 40 million reads) using the TruSeq SBS Kit v4-HS
536 (Illumina, Inc, California, USA).

537 **RNAseq data analysis**

538 The fastq data for the read pairs from the Illumina sequencer has been processed in a bioinformatic workflow.
539 First, the remains of the adapters and sub-standard quality reads have been trimmed with trimmomatic (v0.35).
540 For the pairs in which both reads have passed the trimming, they have been mapped to the respective genome
541 using STAR (v2.7.0a) and indexed BAM files obtained with samtools (v1.9). The reads have been counted using
542 featureCounts from subread package (v1.5.0) with the options for pairs of reads to be counted as RNA fragments.
543 The counting used Ensembl v95 mouse genome annotation GTF file. The count vectors for all the samples have
544 been combined into a count table. The table has been processed in the secondary (statistical) analysis with R
545 scripts using edgeR (v3.24.3), in particular binomial generalized log-linear model with contrast tests. It resulted
546 in lists of genes ranked for differential expression by p-value and used Benjamini-Hochberg adjusted p-value as
547 the estimate of the false discovery rate. Read counts are listed in Supplementary Table 5.

548 **Splicing analysis**

549 All splice events were identified using SplAdder on the aligned RNA-Seq BAM files (Kahles et al., 2016).
550 Gencode release M20 (Mus_musculus.GRCm38.95) was used for identification of slice events. Splice events
551 considered were exon skips, alternative 3'/5', and intron retentions. Only events with highest confidence as
552 defined by SplAdder (level 3) were considered for downstream analyses. All parameters used for the analyses are
553 listed here:

554 *-v y -M merge_graphs -t exon_skip,intron_retention,alt_3prime,alt_5prime -c 3 --ignore_mismatches y*

555 Only events with a minimum of 5 reads and an average expression greater than 20 reads in the flanking exons
556 across all samples were considered in the analysis. All plots and analyses performed on SplAdder output were
557 done in R (version 3.3.3). Intron retention events are listed in Supplementary Table 6.

558 **Statistical analysis**

559 Statistical significance was determined using the statistical tests indicated in the respective figure legends. Data
560 are presented as mean ± SD, if not indicated differently. Mouse studies were not randomized, but were blinded as
561 the analyses were conducted on randomly assigned mouse number, and given to operators without any information

562 until the end of the experiments. Animals of both genders were used and mice with health concerns were excluded
563 from experiments. No inclusion/exclusion criteria were pre-established. No statistical methods were used to
564 predetermine sample size. All experiments are performed at least 3 times if not indicated differently; n refers to
565 the number of biological replicates.

566 **REFERENCES**

567 Alors-Perez, E., Blázquez-Encinas, R., Alcalá, S., Viyuela-García, C., Pedraza-Arevalo, S., and Cabezas-Sainz,
568 P. (2021). Dysregulated splicing factor SF3B1 unveils a dual therapeutic vulnerability to target pancreatic
569 cancer cells and cancer stem cells with an anti-splicing drug. J. Exp. Clin. Cancer Res. 1–37.
570 Alsafadi, S., Houy, A., Battistella, A., Popova, T., Wassef, M., Henry, E., Tirode, F., Constantinou, A., Piperno-
571 Neumann, S., Roman-Roman, S., et al. (2016). Cancer-associated SF3B1 mutations affect alternative splicing
572 by promoting alternative branchpoint usage. Nat. Commun. *7*.
573 Bailey, T. and, and Elkan, C. (1994). Fitting a mixture model by expectation maximization. AAAI Press 3–9.
574 Bhardwaj, V., Heyne, S., Sikora, K., Rabbani, L., Rauer, M., Kilpert, F., Richter, A.S., Ryan, D.P., and Manke,
575 T. (2019). SnakePipes: Facilitating flexible, scalable and integrative epigenomic analysis. Bioinformatics *35*,
576 4757–4759.
577 Boj, S.F., Hwang, C., Baker, L., Chio, C., Engle, D.D., Corbo, V., Jager, M., Ponz-sarvise, M., Tiriac, H.,
578 Spector, M.S., et al. (2015). Organoid Models of Human and Mouse Ductal Pancreatic Cancer. Cell *160*, 324–
579 338.
580 Bolck, H.A., Pauli, C., Göbel, E., Mühlbauer, K., Dettwiler, S., Moch, H., and Schraml, P. (2019). Cancer
581 Sample Biobanking at the Next Level: Combining Tissue With Living Cell Repositories to Promote Precision
582 Medicine. Front. Cell Dev. Biol. *7*, 1–10.
583 Cerami, E., Gao, J., Dogrusoz, U., Gross, B., Sumer, S.O., Aksoy, B.A., Jacobsen, A., Byrne, C., Heuer, M.,
584 Larsson, E., et al. (2017). The cBio Cancer Genomics Portal: An Open Platform for Exploring Multidimensional
585 Cancer Genomics Data. Cancer Discov. *32*, 736–740.
586 Creighton, C.J., Morgan, M., Gunaratne, P.H., Wheeler, D.A., Gibbs, R.A., Robertson, G., Chu, A., Beroukhim,
587 R., Cibulskis, K., Signoretti, S., et al. (2013). Comprehensivemolecular characterization of clear cell renal cell
588 carcinoma. Nature *499*, 43–49.
589 Dahinden, C., Ingold, B., Wild, P., Boysen, G., Luu, V.-D., Montani, M., Kristiansen, G., Sulser, T., Bühlmann,
590 P., Moch, H., et al. (2010). Mining Tissue Microarray Data to Uncover Combinations of Biomarker Expression
591 Patterns that Improve Intermediate Staging and Grading of Clear Cell Renal Cell Cancer Clinical Cancer
592 Research. Clin Cancer Res *16*, 88–98.
593 Darman, R.B., Seiler, M., Agrawal, A.A., Lim, K.H., Peng, S., Aird, D., Bailey, S.L., Bhavsar, E.B., Chan, B.,
594 Colla, S., et al. (2015). Cancer-Associated SF3B1 Hotspot Mutations Induce Cryptic 3' Splice Site Selection

through Use of a Different Branch Point. Cell Rep. *13*, 1033–1045.

Davis, C.F., Ricketts, C.J., Wang, M., Yang, L., Cherniack, A.D., Shen, H., Buhay, C., Kang, H., Kim, S.C., Fahey, C.C., et al. (2014). The somatic genomic landscape of chromophobe renal cell carcinoma. Cancer Cell *26*, 319–330.

Gao, J., Aksoy, B.A., Dogrusoz, U., Dresdner, G., Gross, B., Sumer, S.O., Sun, Y., Jacobsen, A., Sinha, R., Larsson, E., et al. (2014). Integrative Analysis of Complex Cancer Genomics and Clinical Profiles Using the cBioPortal Complementary Data Sources and Analysis Options. Sci Signal *6*, 1–20.

Greenald, D., Jeyakani, J., Pelster, B., Sealy, I., Mathavan, S., and van Eeden, F.J. (2015). Genome-wide mapping of Hif-1aα binding sites in zebrafish. BMC Genomics *16*, 1–17.

Hingorani, S.R., Wang, L., Multani, A.S., Combs, C., Deramaudt, T.B., Hruban, R.H., Rustgi, A.K., Chang, S., and Tuveson, D.A. (2005). Trp53 R172H and Kras G12D cooperate to promote chromosomal instability and widely metastatic pancreatic ductal adenocarcinoma in mice. Cancer Cell *7*, 469–483.

Hruban, R.H., Adsay, N.V., Albores-Saavedra, J., Anver, M.R., Biankin, A. V., Boivin, G.P., Furth, E.E., Furukawa, T., Klein, A., Klimstra, D.S., et al. (2006). Pathology of genetically engineered mouse models of pancreatic exocrine cancer: Consensus report and recommendations. Cancer Res. *66*, 95–106.

Huch, M., Bonfanti, P., Boj, S.F., Sato, T., Loomans, C.J.M., Van De Wetering, M., Sojoodi, M., Li, V.S.W., Schuijers, J., Gracanin, A., et al. (2013). Unlimited in vitro expansion of adult bi-potent pancreas progenitors through the Lgr5/R-spondin axis. EMBO J. *32*, 2708–2721.

Jiménez-Vacas, J.M., Herrero-Aguayo, V., Gómez-Gómez, E., León-González, A.J., Sáez-Martínez, P., Alors-Pérez, E., Fuentes-Fayos, A.C., Martínez-López, A., Sánchez-Sánchez, R., González-Serrano, T., et al. (2019). Spliceosome component SF3B1 as novel prognostic biomarker and therapeutic target for prostate cancer. Transl. Res. *212*, 89–103.

Kahles, A., Ong, C.S., Zhong, Y., and Rätsch, G. (2016). SplAdder: Identification, quantification and testing of alternative splicing events from RNA-Seq data. Bioinformatics *32*, 1840–1847.

Kahles, A., Lehmann, K. Van, Toussaint, N.C., Hüser, M., Stark, S.G., Sachsenberg, T., Stegle, O., Kohlbacher, O., Sander, C., Caesar-Johnson, S.J., et al. (2018). Comprehensive Analysis of Alternative Splicing Across Tumors from 8,705 Patients. Cancer Cell *34*, 211-224.e6.

Koong, A.C., Mehta, V.K., Le, Q.T., Fisher, G.A., Terris, D.J., Brown, J.M., Bastidas, A.J., and Vierra, M. (2000). Pancreatic tumors show high levels of hypoxia. Int. J. Radiat. Oncol. Biol. Phys. *48*, 919–922.

Lieu, Y.K., Liu, Z., Ali, A.M., Wei, X., Penson, A., Zhang, J., An, X., Rabadan, R., Raza, A., Manley, J.L., et

al. (2020). SF3B1 mutant-induced missplicing of MAP3K7 causes anemia in myelodysplastic syndromes. BioRxiv 2020.06.24.169052.

Liu, B., Liu, Z., Chen, S., Ki, M., Erickson, C., Reis-Filho, J.S., Durham, B.H., Chang, Q., De Stanchina, E., Sun, Y., et al. Mutant SF3B1 promotes AKT and NF-kB driven mammary tumorigenesis.

Liu, B., Liu, Z., Chen, S., Ki, M., Erickson, C., Reis-Filho, J.S., Durham, B.H., Chang, Q., De Stanchina, E., Sun, Y., et al. (2020). Mutant SF3B1 promotes AKT and NF-kB driven mammary tumorigenesis. J. Clin. Invest.

López-Cánovas, J.L., del Rio-Moreno, M., García-Fernandez, H., Jiménez-Vacas, J.M., Moreno-Montilla, M.T., Sánchez-Frias, M.E., Amado, V., L-López, F., Fondevila, M.F., Ciria, R., et al. (2021). Splicing factor SF3B1 is overexpressed and implicated in the aggressiveness and survival of hepatocellular carcinoma. Cancer Lett. *496*, 72–83.

Lun, A.T.L., and Smyth, G.K. (2015). Csaw: A Bioconductor package for differential binding analysis of ChIP-seq data using sliding windows. Nucleic Acids Res. *44*, e45.

Mirtschink, P., Krishnan, J., Grimm, F., Sarre, A., Hörl, M., Kayikci, M., Fankhauser, N., Christinat, Y., Cortijo, C., Feehan, O., et al. (2015). HIF-driven SF3B1 induces KHK-C to enforce fructolysis and heart disease. Nature *522*, 444–449.

Muz, B., de la Puente, P., Azab, F., and Azab, A.K. (2015). The role of hypoxia in cancer progression, angiogenesis, metastasis and resistance to therapy. Hypoxia *3*, 83–92.

Obeng, E.A., Chappell, R.J., Seiler, M., Chen, M.C., Campagna, D.R., Schmidt, P.J., Schneider, R.K., Lord, A.M., Wang, L., Gambe, R.G., et al. (2016a). Physiologic Expression of Sf3b1K700E Causes Impaired Erythropoiesis, Aberrant Splicing, and Sensitivity to Therapeutic Spliceosome Modulation. Cancer Cell *30*, 404–417.

Obeng, E.A., Chappell, R.J., Seiler, M., Chen, M.C., Campagna, D.R., Schmidt, P.J., Schneider, R.K., Lord, A.M., Wang, L., Gambe, R.G., et al. (2016b). Physiologic Expression of Sf3b1K700E Causes Impaired Erythropoiesis, Aberrant Splicing, and Sensitivity to Therapeutic Spliceosome Modulation. Cancer Cell *30*, 404–417.

Ohashi, R., Schraml, P., Batavia, A., Angori, S., Simmler, P., Rupp, N., Ajioka, Y., Oliva, E., and Moch, H. (2019). Allele Loss and Reduced Expression of CYCLOPS Genes is a Characteristic Feature of Chromophobe Renal Cell Carcinoma. Transl. Oncol. *12*, 1131–1137.

Ohta, A., Diwanji, R., Kini, R., Subramanian, M., Ohta, A., and Sitkovsky, M. (2011). In vivo T cell activation in lymphoid tissues is inhibited in the oxygen-poor microenvironment. Front. Immunol. *2*.

655 Paolella, B.R., Gibson, W.J., Urbanski, L.M., Alberta, J.A., Zack, T.I., Bandopadhayay, P., Nichols, C.A.,
656 Agarwalla, P.K., Brown, M.S., Lamothe, R., et al. (2017). Copy-number and gene dependency analysis reveals
657 partial copy loss of wild-type SF3B1 as a novel cancer vulnerability. Elife *6*, 1–28.
658 Popli, P., Richters, M.M., Chadchan, S.B., Kim, T.H., Tycksen, E., Griffith, O., Thaker, P.H., Griffith, M., and
659 Kommagani, R. (2020). Splicing factor SF3B1 promotes endometrial cancer progression via regulating KSR2
660 RNA maturation. Cell Death Dis. *11*, 1–13.
661 Quesada, V., Conde, L., Villamor, N., Ordóñez, G.R., Jares, P., Bassaganyas, L., Ramsay, A.J., Beà, S., Pinyol,
662 M., Martínez-Trillos, A., et al. (2012). Exome sequencing identifies recurrent mutations of the splicing factor
663 SF3B1 gene in chronic lymphocytic leukemia. Nat. Genet. *44*, 47–52.
664 Semenza, G.L. (2003). Targeting HIF-1 for cancer therapy. Nat. Rev. Cancer *3*, 721–732.
665 Semenza, G.L. (2019). Pharmacologic targeting of hypoxia-inducible factors. Annu. Rev. Pharmacol. Toxicol.
666 *59*, 379–403.
667 Shalem, O., Sanjana, E.N., Hartenian, E., and Zhang, F. (2014). Genome-Scale CRISPR-Cas9 Knockout.
668 Science *343*, 84–88.
669 Struckmann, K., Mertz, K., Steu, S., Storz, M., Staller, P., Krek, W., Schraml, P., and Moch, H. (2008). pVHL
670 co-ordinately regulates CXCR4/CXCL12 and MMP2/MMP9 expression in human clear-cell renal cell
671 carcinoma. J. Pathol. *214*, 464–471.
672 Uhlen, M., Zhang, C., Lee, S., Sjöstedt, E., Fagerberg, L., Bidkhori, G., Benfeitas, R., Arif, M., Liu, Z., Edfors,
673 F., et al. (2017). A pathology atlas of the human cancer transcriptome. Science *357*, 660–671.
674 Wahl, M.C., Will, C.L., and Lührmann, R. (2009). The Spliceosome: Design Principles of a Dynamic RNP
675 Machine. Cell *136*, 701–718.
676 Yoshida, K., and Ogawa, S. (2014). Splicing factor mutations and cancer. Wiley Interdiscip. Rev. RNA *5*, 445–
677 459.
678 Zhang, L., Zhang, X., Zhang, H., Liu, F., Bi, Y., Zhang, Y., Cheng, C., and Liu, J. (2020). Knockdown of
679 SF3B1 inhibits cell proliferation, invasion and migration triggering apoptosis in breast cancer via aberrant
680 splicing. Breast Cancer *27*, 464–476.
681 Zhang, Y., Liu, T., Meyer, C.A., Eeckhoute, J., Johnson, D.S., Bernstein, B.E., Nussbaum, C., Myers, R.M.,
682 Brown, M., Li, W., et al. (2008). Model-based analysis of ChIP-Seq (MACS). Genome Biol. *9*.
683

Figure 1

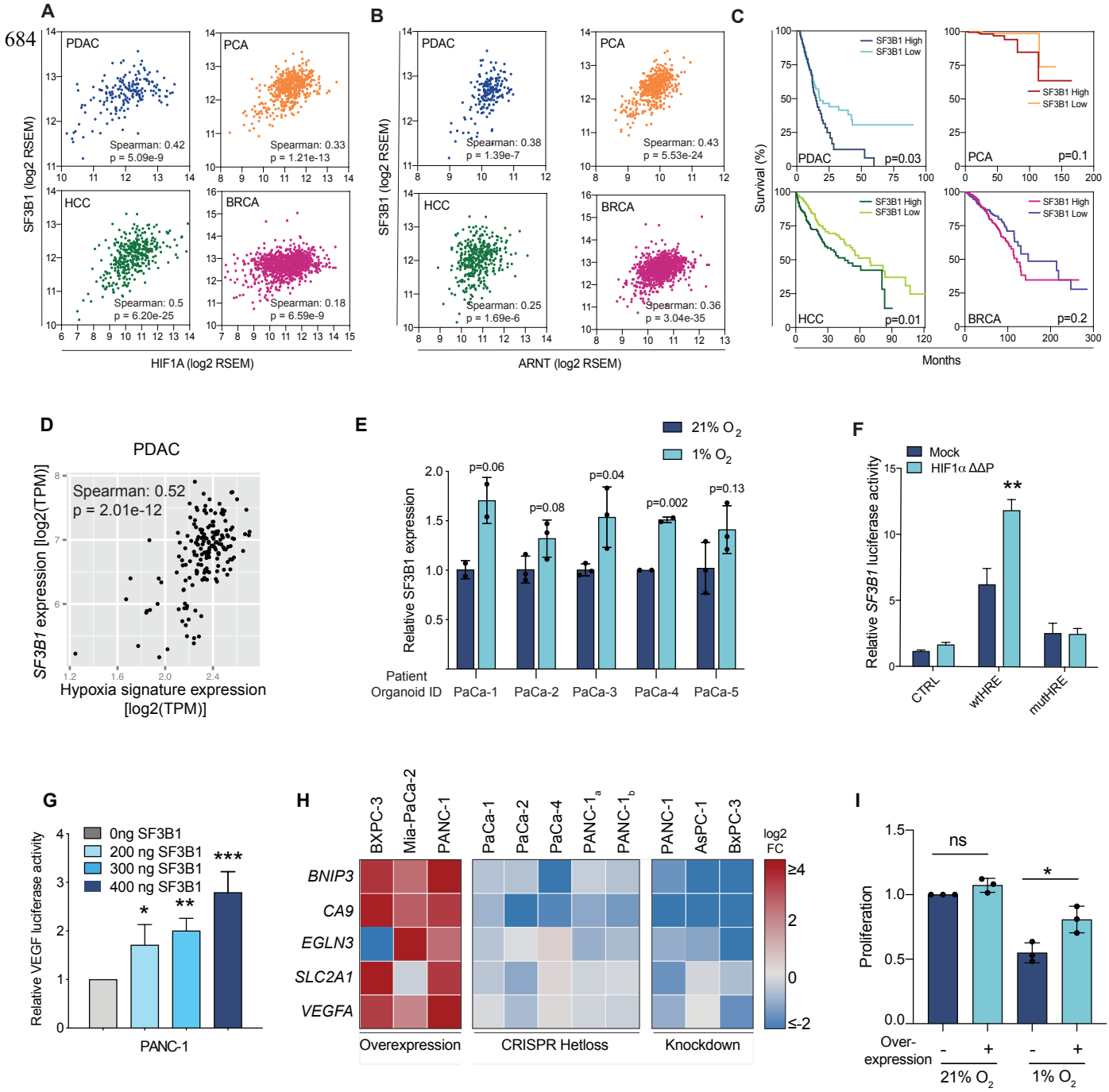
A
PDAC
Spearman: 0.42
p = 5.09e-9
PCA
Spearman: 0.33
p = 1.21e-13
HCC
Spearman: 0.5
p = 6.20e-25
BRCA
Spearman: 0.18
p = 6.59e-9
SF3B1 (log2 RSEM)
HIF1A (log2 RSEM)
B
PDAC
Spearman: 0.38
p = 1.39e-7
PCA
Spearman: 0.43
p = 5.53e-24
HCC
Spearman: 0.25
p = 1.69e-6
BRCA
Spearman: 0.36
p = 3.04e-35
SF3B1 (log2 RSEM)
ARNT (log2 RSEM)
C
SF3B1 High
SF3B1 Low
PDAC p=0.03
PCA p=0.1
HCC p=0.01
BRCA p=0.2
Survival (%)
Months
D
PDAC
Spearman: 0.52
p = 2.01e-12
SF3B1 expression [log2(TPM)]
Hypoxia signature expression [log2(TPM)]
E
21% O2
1% O2
p=0.06
p=0.08
p=0.04
p=0.002
p=0.13
Relative SF3B1 expression
Patient Organoid ID
PaCa-1
PaCa-2
PaCa-3
PaCa-4
PaCa-5
F
Mock
HIF1α ΔΔP
Relative SF3B1 luciferase activity
CTRL
wtHRE
muHRE
G
0ng SF3B1
200 ng SF3B1
300 ng SF3B1
400 ng SF3B1
Relative VEGF luciferase activity
PANC-1
H
BXPC-3
Mia-PaCa-2
PANC-1
PaCa-1
PaCa-2
PaCa-4
PANC-1a
PANC-1b
PANC-1
AsPC-1
BxPC-3
log2 FC
BNIP3
CA9
EGLN3
SLC2A1
VEGFA
Overexpression
CRISPR Hetloss
Knockdown
I
ns
Proliferation
Over-expression
21% O2
1% O2

685 **Figure 1. SF3B1 is required for efficient HIF signalling. (A and B)** Scatter plot showing the correlation of
686 *SF3B1* and *HIF1A* (A) and *HIF1B* (B) expression in PDAC, prostate cancer (PCA), hepatocellular carcinoma
687 (HCC) and breast cancer (BRCA). The significance of the correlation in is indicated by its p-value. (**C)** Survival
688 of patients was stratified according to the median *SF3B1* expression in the indicated cancer types. P-values were
689 computed with a Log-rank (Mantel-Cox) test. **(D)** Scatter plot showing the correlation between *SF3B1* mRNA
690 levels and a hypoxia signature in PDAC patients, which is represented by the mean expression value (TPM) of
691 34 HIF-target genes. **(E)** SF3B1 expression in a panel of human patient-derived PDAC organoids exposed to
692 1% O_2 for 12 hours. Error bars indicate standard deviation (S.D.) of biological replicates. Two-tailed unpaired t-
693 test was used to compute the indicated p-values. **(F)** Transfection of a wildtype (WT) or HRE-mutated *SF3B1*
694 promoter-luciferase reporter (mutHRE = AAAAA) together with either an empty vector control, or HIF1αΔΔP
695 in PANC-1 cells. Data are shown as mean ± S.D. of biological replicates (n=3). ** P<0.01 normalized to mock
696 wtHRE, two-tailed unpaired t-test. **(G)** Transfection of a *VEGF* promoter-luciferase reporter alone or together
697 with either HIF1αΔΔP (the constitutively active form of HIF1α), or in combination with different concentrations
698 of SF3B1 plasmid in PANC-1 cells. Data are shown as mean ± S.D. of biological replicates (n=3). *<P0.05,
699 **P<0.01, ***P<0.001. One-way ANOVA followed by a Dunnet's multiple comparison post-test. **(H)** Heatmap
700 showing the expression of various HIF1α-target genes in patient-derived PDAC organoid lines and commercial
701 PDAC cell lines after overexpression or knockdown of *SF3B1*, either with CRISPR-Cas9 or siRNA exposed to
702 hypoxia for 12 hours. The indicated fold-changes are relative to the following controls: Transfection with an
703 empty-vector (overexpression), the respective unedited cell line (CRISPR-hetloss) or treatment with control
704 siRNA (knockdown). Expression levels are relative to the housekeeping gene *TBP*. For PANC-1, usage of two
705 distinct guide RNAs are indicated by subscripted *a* and *b*. For each cell line and its respective control, the
706 experiment was performed at least three times. **(I)** Impact of SF3B1 overexpression in MiaPaCa-2 cells cultured
707 in normoxia or hypoxia for 48 hours relative to normoxic control cells (=3). *<P0.05, two-tailed unpaired t-test.

Figure 2

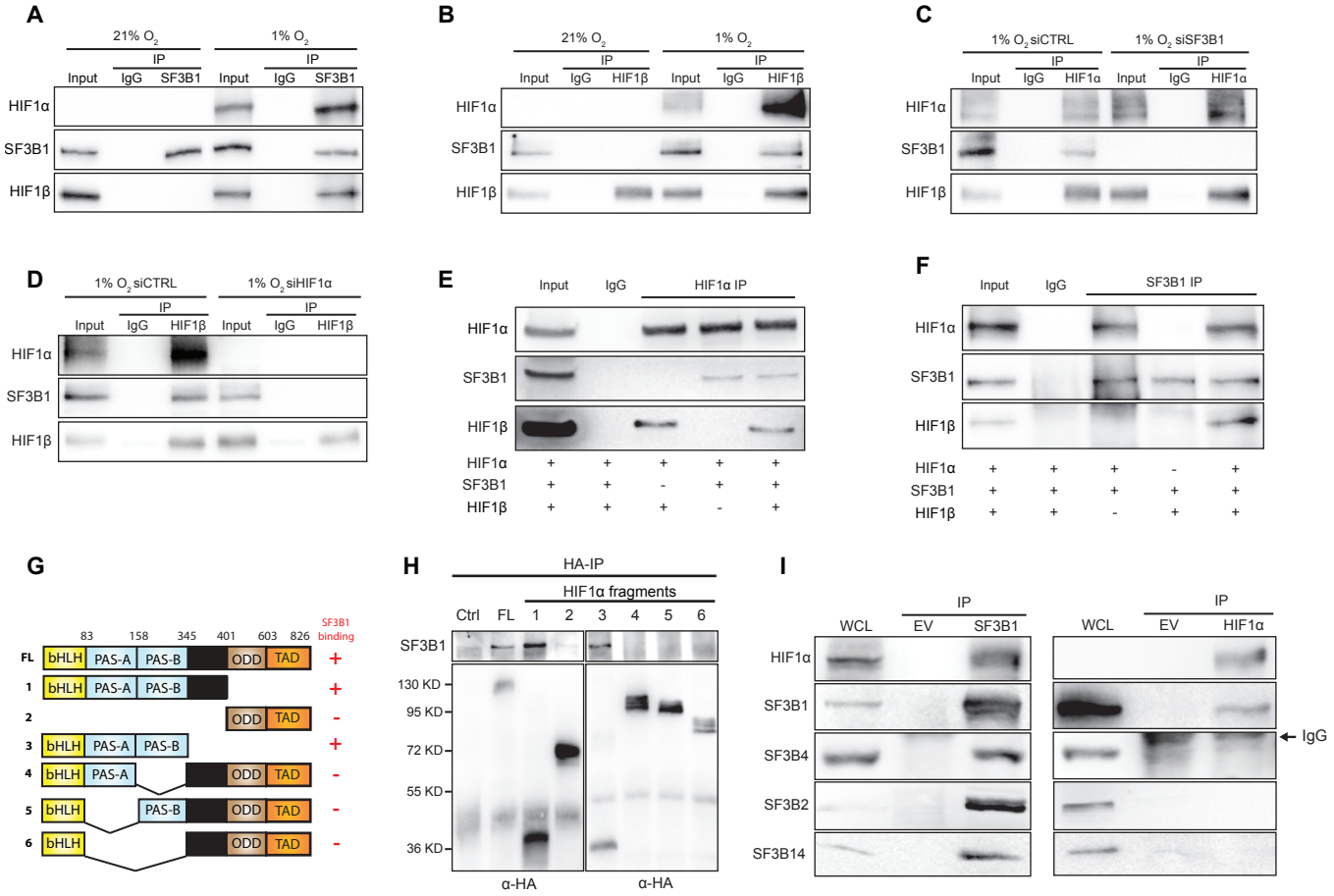
A
21% O2
1% O2
IP
Input
IgG
SF3B1
HIF1α
SF3B1
HIF1β
B
HIF1β
C
1% O2 siCTRL
1% O2 siSF3B1
HIF1α
D
1% O2 siHIF1α
E
HIF1α IP
F
SF3B1 IP
G
83
158
345
401
603
826
SF3B1 binding
FL
bHLH
PAS-A
PAS-B
ODD
TAD
H
HA-IP
HIF1α fragments
Ctrl
FL
130 KD
95 KD
72 KD
55 KD
36 KD
α-HA
I
WCL
EV
SF3B4
SF3B2
SF3B14
IgG

708 **Figure 2. SF3B1 physically interacts with HIF1α.** **(A)** Protein extracts from HEK293T cells exposed to 21%
709 or 1% O_2 for 12 hours were subjected to immunoprecipitation (IP) with an anti-SF3B1 antibody or anti-mouse
710 IgG and processed for immunoblotting for indicated proteins. **(B)** Protein extracts from HEK293T cells exposed
711 to 21% or 1% O_2 for 12 hours were subjected to IP with an anti-HIF1β antibody or anti-mouse IgG and processed
712 for immunoblotting for indicated proteins. **(C)** Protein extracts from HEK293T cells transfected with the indicated
713 siRNAs, exposed to 1% O_2 for 12 hours, were subjected to IP with an anti-HIF1α antibody or anti-rabbit IgG and
714 processed for immunoblotting for indicated proteins. **(D)** Protein extracts from HEK293T cells transfected with
715 the indicated siRNAs, exposed to 1% O_2 for 12 hours, were subjected to IP with an anti-HIF1β antibody or anti-
716 rabbit IgG and processed for immunoblotting for indicated proteins. **(E)** Recombinant strep-tagged HIF1α, SF3B1
717 and HIF1β proteins purified from Sf9 insect cells were mixed and subjected to IP using an anti-HIF1α antibody
718 or anti-rabbit IgG as control and processed for immunoblotting for indicated proteins. (+) means that the indicated
719 recombinant protein was added to the IP, (-) means that the indicated recombinant protein was omitted from the
720 IP. **(F)** Recombinant strep-tagged HIF1α, SF3B1 and HIF1β proteins were subjected to IP using an anti-SF3B1
721 antibody or anti-mouse IgG as control and processed for immunoblotting for indicated proteins. (+) means that
722 the recombinant protein was added to the IP, (-) means that the recombinant protein was omitted from the IP. **(G)**
723 Schematic of full-length HIF1α and corresponding deletion mutants (numbered 1-6) used in IP experiments with
724 an anti-SF3B1 antibody. (+) and (-) signs denote SF3B1 binding (experimental data are displayed in Fig. 2H).
725 bHLH: basic helix-loop-helix, PAS-A and PAS-B: Per-ARNT-Sim domains, ODD: oxygen-dependent
726 degradation domain and TAD: transactivation domain. **(H)** HEK293T cells were transfected with a HA-tagged
727 WT full length (FL) or mutant forms of HIF1α (1-6). Lysates were then processed for immunoprecipitation with
728 an anti-HA antibody (HA-IP) followed by immunoblotting with an anti-HA antibody. **(I)** Protein extracts from
729 HEK293T cells exposed to 1% O_2 for 8 hours were subjected to IP, with an anti-SF3B1 antibody or an anti-mouse
730 IgG (left), or with an anti-HIF1α antibody and an anti-rabbit IgG (right). All samples were processed for
731 immunoblotting for indicated proteins. The arrow on the right indicates the IgG band.

Figure 3

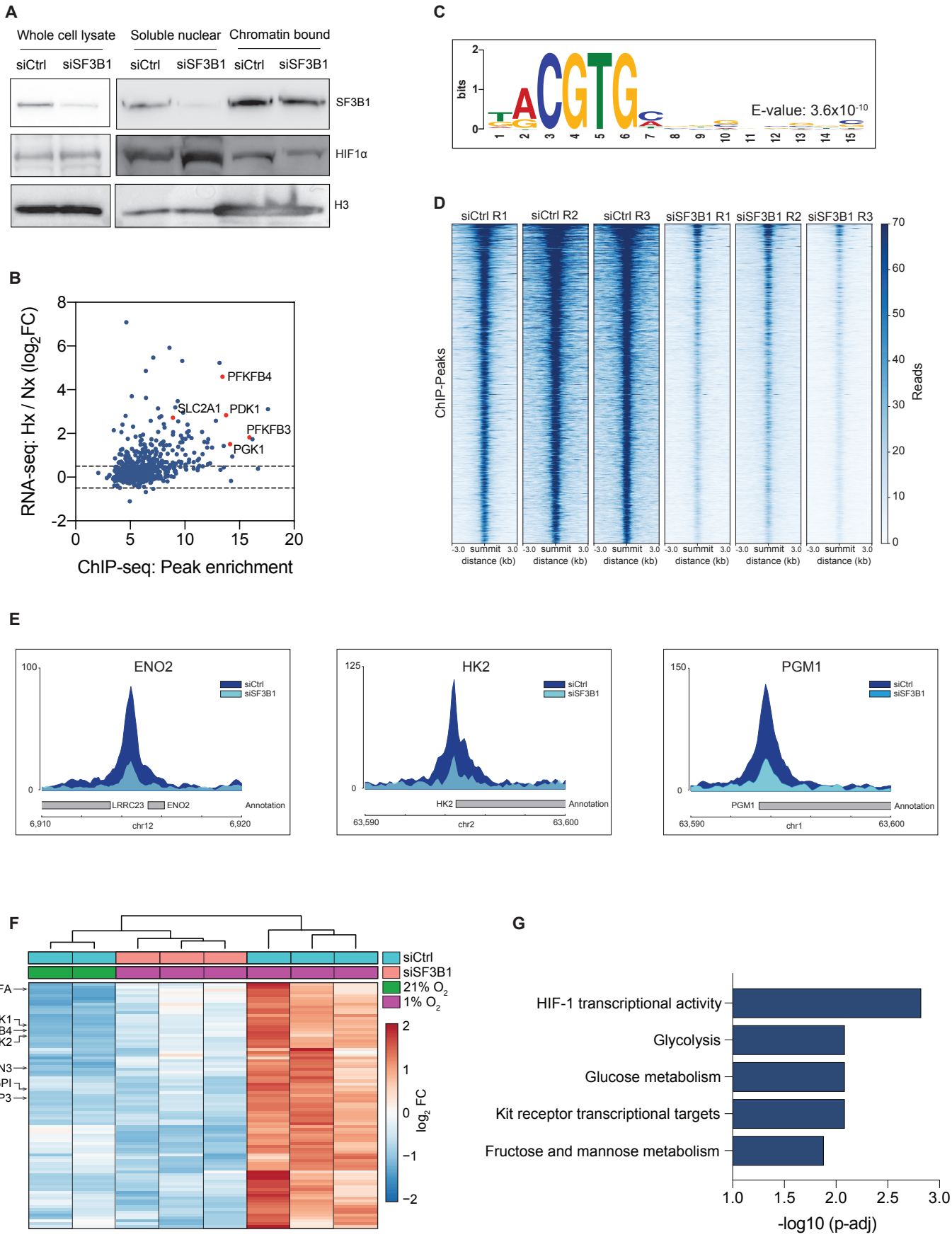
A
Whole cell lysate
Soluble nuclear
Chromatin bound
siCtrl
siSF3B1
siCtrl
siSF3B1
siCtrl
siSF3B1
SF3B1
HIF1α
H3
B
RNA-seq: Hx / Nx (log2FC)
ChIP-seq: Peak enrichment
PFKFB4
SLC2A1
PDK1
PFKFB3
PGK1
C
bits
E-value: 3.6x10-10
D
siCtrl R1
siCtrl R2
siCtrl R3
siSF3B1 R1
siSF3B1 R2
siSF3B1 R3
ChIP-Peaks
Reads
summit
distance (kb)
E
ENO2
HK2
PGM1
siCtrl
siSF3B1
LRRC23
ENO2
HK2
PGM1
Annotation
chr12
chr2
chr1
F
siCtrl
siSF3B1
21% O2
1% O2
VEGFA
PDK1
PFKFB4
HK2
EGLN3
GPI
BNIP3
log2 FC
G
HIF-1 transcriptional activity
Glycolysis
Glucose metabolism
Kit receptor transcriptional targets
Fructose and mannose metabolism
-log10 (p-adj)

732 **Figure 3. SF3B1 is essential for binding of HIF1α to its target genes. (A)** Subcellular protein fractionation
733 experiment in PANC-1 cells treated with control siRNA (siCtrl) or an siRNA targeting *SF3B1* (siSF3B1) and
734 incubated in 1% O_2 for 8 hours. SF3B1, HIF1α and H3 isolated from the indicated fractions are immunoblotted.
735 (**B**) Enrichment of peaks identified by HIF1α-ChIP-seq plotted against the increase in expression levels (normoxia
736 vs 1% O_2 for 8 hours) of the corresponding nearest genes as measured by RNA-seq. **(C)** Identification of the HRE-
737 motif (RCGTG) by MEME motif-analysis of the ChIP-seq peaks in siCtrl-treated PANC-1 cells. Nucleotide
738 sequences of 100 bases surrounding the peak summits were analysed, representative result of one replicate is
739 shown. **(D)** HIF1α-ChIP-seq reads of all identified peaks (n=740) of PANC-1 cells treated either with siCtrl or
740 siSF3B1. **(E)** Peak-enrichment of the transcription start site of ENO2, HK2 and PGM2 in PANC-1 cells treated
741 either with siCtrl or siSF3B1. Representative data from corresponding experimental replicates is shown. **(F)**
742 Heatmap depicting nearest genes of HIF1α-ChIP-seq peaks that are upregulated in hypoxia (FC>0.5, FDR<0.1)
743 and downregulated in siSF3B1 treated PANC-1 cells (FC<-0.5, FDR<0.1). **(G)** Pathway analysis of the gene-set
744 shown in (F) based on the BioPlanet database. Pathways are ranked according to the adjusted P-value (p-adj).

Figure 4

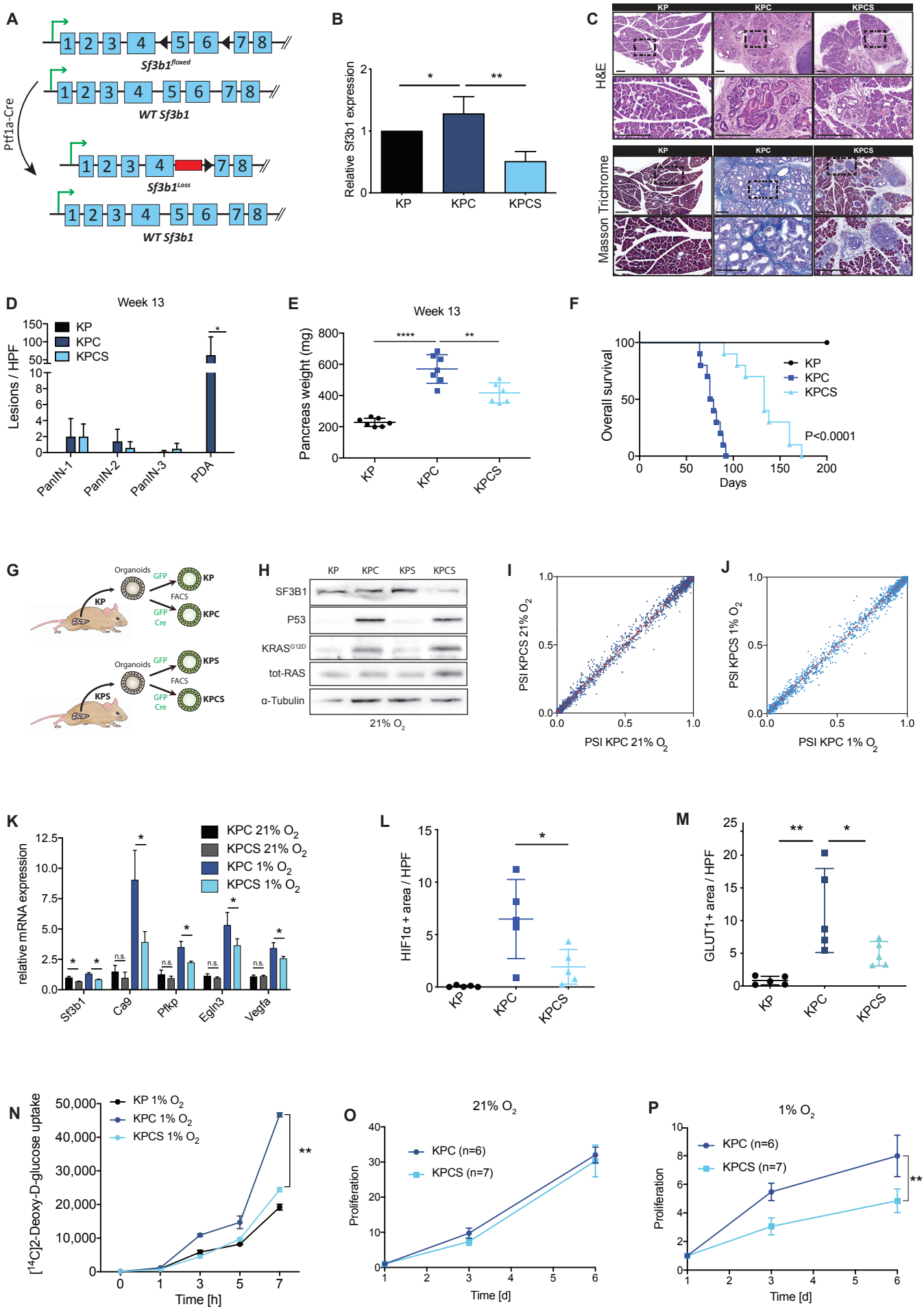
A
Sf3b1floxed
Ptf1a-Cre
WT Sf3b1
Sf3b1Loss
WT Sf3b1
B
Relative Sf3b1 expression
KP
KPC
KPCS
C
KP
KPC
KPCS
H&E
Masson Trichrome
D
Week 13
Lesions / HPF
KP
KPC
KPCS
PanIN-1
PanIN-2
PanIN-3
PDA
E
Week 13
Pancreas weight (mg)
F
Overall survival
Days
P<0.0001
G
Organoids
GFP
FACS
GFP Cre
KP
KPC
KPS
KPCS
H
SF3B1
P53
KRASG12D
tot-RAS
α-Tubulin
21% O2
I
PSI KPCS 21% O2
PSI KPC 21% O2
J
PSI KPCS 1% O2
PSI KPC 1% O2
K
relative mRNA expression
KPC 21% O2
KPCS 21% O2
KPC 1% O2
KPCS 1% O2
Sf3b1
Ca9
Pfkp
Egln3
Vegfa
L
HIF1α + area / HPF
M
GLUT1+ area / HPF
N
[14C]2-Deoxy-D-glucose uptake
KP 1% O2
KPC 1% O2
KPCS 1% O2
Time [h]
O
21% O2
Proliferation
KPC (n=6)
KPCS (n=7)
Time [d]
P
1% O2
Proliferation
KPC (n=6)
KPCS (n=7)
Time [d]

745 **Figure 4. Heterozygosity of *Sf3b1* hampers PDAC progression through impaired HIF-signalling. (A)**
746 Schematic representation of the transgenic approach to obtain pancreas-specific heterozygosity of Sf3b1. **(B)**
747 qPCR analysis of *Sf3b1* mRNAs from pancreata of KP, KPC and KPCS mice of 13 weeks of age. For *P<0.05
748 **P<0.01. One-way ANOVA followed by a Tukey's multiple comparison post-test. **(C)** Representative images
749 of H&E staining and Masson's Trichrome staining showing histopathologic lesions in pancreata of KP, KPC and
750 KPCS mice at 13 weeks of age. Dashed lines indicate the area magnified below. Scale bar is 100 μm. **(D)**
751 Quantification of the prevalence of mPanIN and PDAC in the H&E-stained pancreatic sections of 13-week-old
752 KP, KPC and KPCS mice. Ten high power fields (HPF) were analysed per animal. Data are represented as mean
753 ± S.D. (n = 5). * P<0.05, ** P<0.01, *** P<0.001. One-way ANOVA followed by a Tukey's multiple comparison
754 post-test. **(E)** Pancreas weight of 13 weeks old KP, KPC and KPCS mice. The data are represented as mean ±
755 S.D. (n = 6-7). ** P<0.01, **** P<0.0001. One-way ANOVA followed by a Tukey's multiple comparison post-
756 test. **(F)** Kaplan-Meier survival curve of KP, KPC and KPCS mice over time (KP n = 8, KPC n = 10, KPCS n =
757 10). Long rank test. **(G)** Schematic representation of the generation of murine tumor organoids with GFP or GFP-
758 Cre viruses derived from KP and KPS mice. Expression of Cre recombinase in KPC and KPCS organoids leads
759 to the activation of $Kras^{G12D}$ and $Trp53^{R17H}$ and to a loss of one allele of *Sf3b1* in KPCS organoids. **(H)** Protein
760 extracts from KP, KPC, KPS, and KPCS organoids grown under normoxic conditions were immunoblotted for
761 the indicated proteins. **(I and J)** Scatter plot of percent spliced-in (PSI) events in KPC and KPCS organoids
762 cultured in normoxia (G) and hypoxia (H), representing a measure of high confidence alternative splice events (n
763 ≥ 4 organoid lines, lines established from individual mice). **(K)** Expression levels of HIF1α target genes
764 determined by qPCR of KPC and KPCS organoids (n = 6 organoid lines) cultured in normoxia and hypoxia for
765 48 hours. Expression levels are relative to the housekeeping gene *Actb*. Data are shown as mean ± SEM. For each
766 organoid line, the experiment was performed in three biological replicates. * P<0.05, One-way ANOVA followed
767 by a Tukey's multiple comparison post-test. **(L and M),** Quantification of HIF1α (L) or GLUT1 (M) positive
768 areas in KP, KPC and KPCS mice at 13 weeks of age. Ten high power fields (HPF) were analysed per animal (n
769 = 5). * P<0.05. One-way ANOVA followed by a Tukey's multiple comparison post-test. (**N**) KPC and KPCS
770 organoids were incubated in medium containing [^{14}C] 2-deoxyglucose at different time-points and processed for
771 glucose uptake measurements. Organoids were exposed to 1% O_2 for 12 hours. Counts were normalized to the
772 cell number (*n* = 4 biological replicates per time point and condition). ** P<0.01, One-way ANOVA followed by
773 a Tukey's multiple comparison post-test. **(O and P)** Proliferation of organoids in normoxia (O) and hypoxia (P).
774 Data are shown as mean ± SEM of organoid lines (n ≥ 6 organoid lines). For each organoid line, the experiment
775 was performed in three biological replicates. ** P<0.01, indicating comparison of KPC and KPCS, Two-way
776 ANOVA followed by a Sidak's multiple comparisons test.

Figure 5

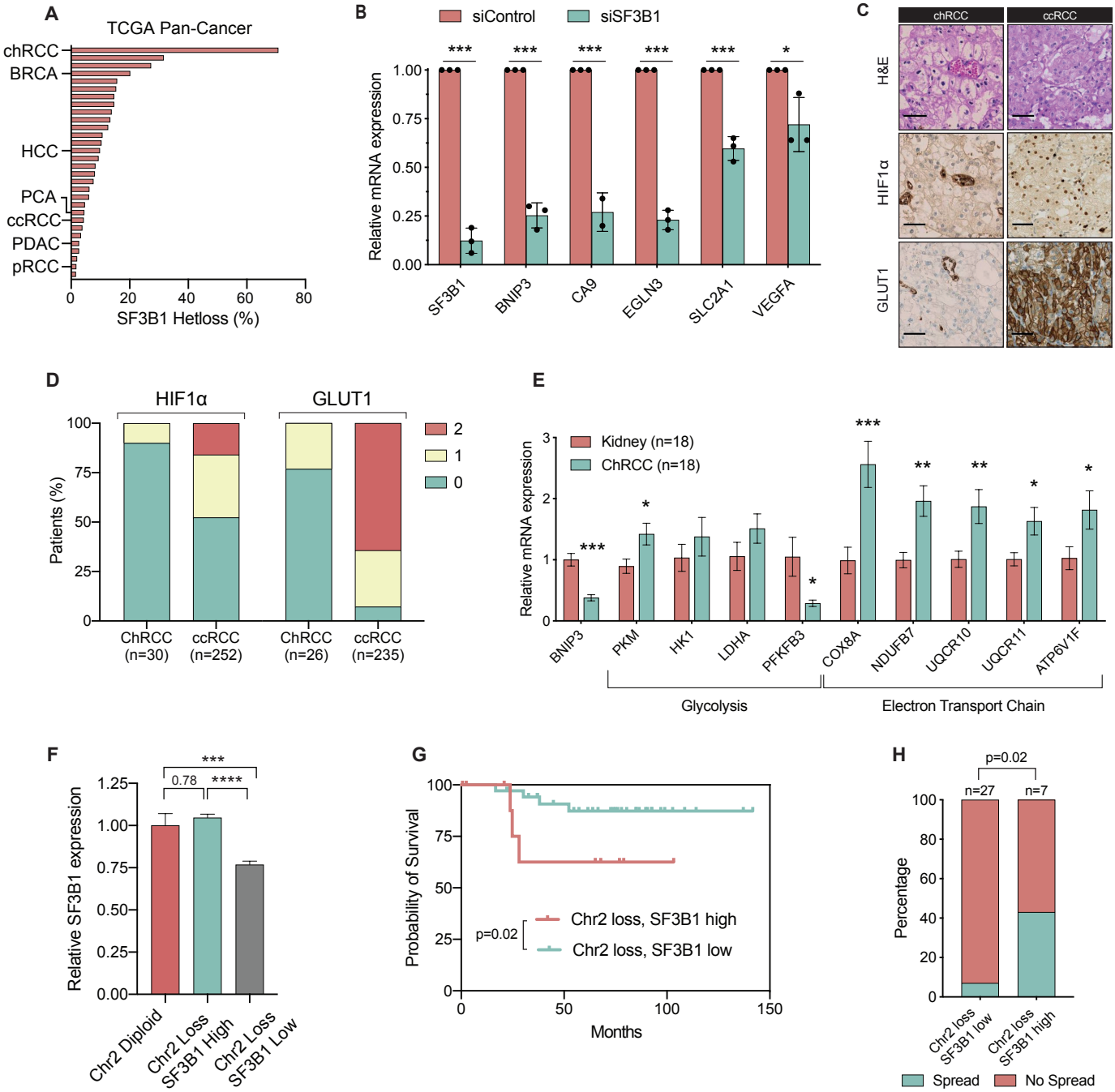
A
TCGA Pan-Cancer
chRCC
BRCA
HCC
PCA
ccRCC
PDAC
pRCC
0
20
40
60
80
SF3B1 Hetloss (%)
B
siControl
siSF3B1
Relative mRNA expression
1.00
0.75
0.50
0.25
0.00
SF3B1
BNIP3
CA9
EGLN3
SLC2A1
VEGFA
C
chRCC
ccRCC
H&E
HIF1α
GLUT1
D
HIF1α
GLUT1
Patients (%)
100
75
50
25
0
2
1
0
ChRCC (n=30)
ccRCC (n=252)
ChRCC (n=26)
ccRCC (n=235)
E
Kidney (n=18)
ChRCC (n=18)
Relative mRNA expression
BNIP3
PKM
HK1
LDHA
PFKFB3
COX8A
NDUFB7
UQCR10
UQCR11
ATP6V1F
Glycolysis
Electron Transport Chain
F
Relative SF3B1 expression
1.25
1.00
0.75
0.50
0.25
0.00
0.78
Chr2 Diploid
Chr2 Loss SF3B1 High
Chr2 Loss SF3B1 Low
G
Probability of Survival
100
75
50
25
0
p=0.02
Chr2 loss, SF3B1 high
Chr2 loss, SF3B1 low
0
50
100
150
Months
H
p=0.02
n=27
n=7
Percentage
100
80
60
40
20
0
Chr2 loss SF3B1 low
Chr2 loss SF3B1 high
Spread
No Spread

Figure 5. ChRCC with heterozygous SF3B1 loss grows in a normoxic environment. (A) Loss of heterozygosity (LOH) of SF3B1 in 30 solid tumors of the TCGA Pan-Cancer Atlas. Highlighted are the tumor types analysed in Fig 1 A-C, as well as chRCC and ccRCC. The full list is provided in Suppl. Table 2 **(B)** qPCR analysis of indicated genes in patient-derived cell chRCC cells treated with siControl or siSF3B1 under 1% O_2 for 8 hours. Data represents results of three independent experiments. Expression levels are relative to the housekeeping gene *TBP*. * P<0.05, *** P<0.001, two-tailed unpaired t-test. **(C)** Representative H&E and IHC staining of HIF1α and GLUT1 of ccRCC and chRCC patients, scale bar is 50µm. **(D)** Quantification of HIF1α and GLUT1 staining in ccRCC and chRCC patients, categorized as intense (2), weak (1) or no detectable (0) staining. **(E)** qPCR analysis of genes involved in glycolysis and oxidative phosphorylation in chRCC tumors (n = 18) and matched kidney tissue (n = 18). Expression levels are relative to *TBP*. * P<0.05, ** P<0.01, *** P<0.001, two-tailed unpaired t-test. **(F)** Relative SF3B1 expression of the stratified TCGA-cohort. *** P<0.001, **** P<0.0001. One-way ANOVA followed by a Tukey's multiple comparison post-test. **(G)** Survival of patients (TCGA cohort) stratified according to chromosome 2 status and SF3B1 expression as indicated. P-value was computed with a Log-rank (Mantel-Cox) test. **(H)** Percentage of chRCC patients (TCGA cohort) where spreading to lymph nodes was observed. Patients lacking information of lymph node status were omitted for analysis. Significance was computed with chi-square tests.

Figure 6

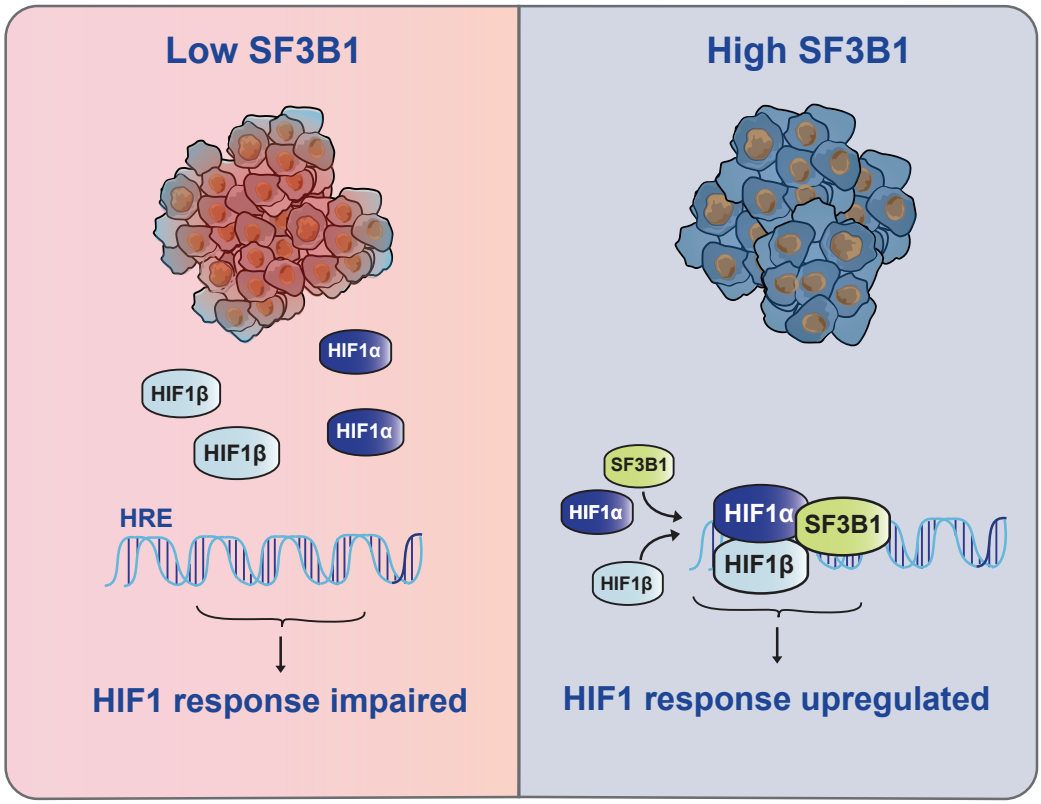

Figure 6. Model of HIF1 activation by SF3B1. If SF3B1 levels are low, HIF1-complex does not bind efficiently to its DNA-targets, resulting in insufficient HIF1 response and impaired metabolic adaption to hypoxia (left). When SF3B1 levels are high, a heterotrimeric HIF1 complex is formed, allowing enhanced DNA-binding and transcription of hypoxia responsive genes, resulting in metabolic adaption to hypoxia (right).

Supplementary Figure 1

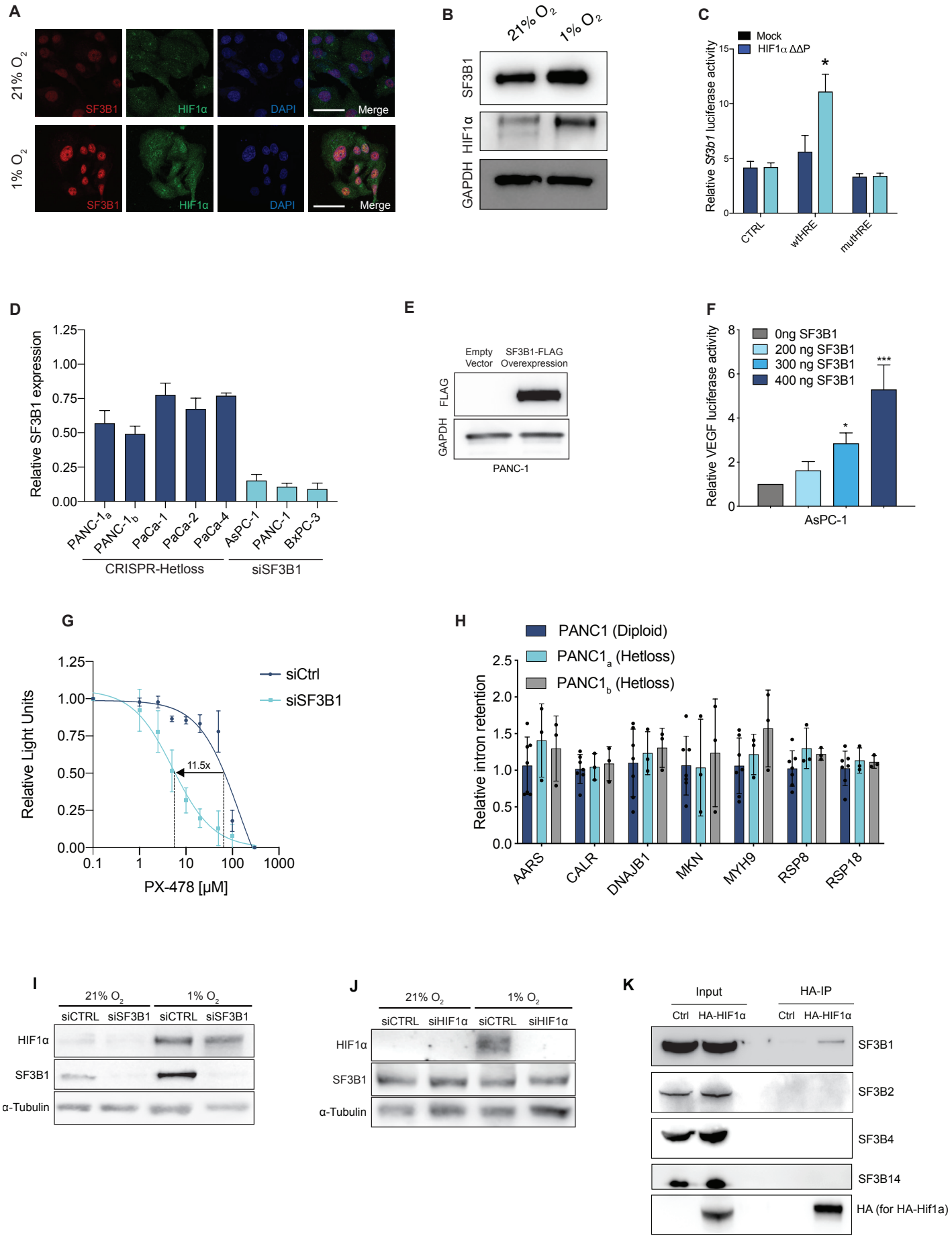

793 **Supplementary Figure 1. Effects of SF3B1 reduction on HIF-response. (A)** Immunofluorescence images of
794 PANC-1 cells grown in 21% O_2 or 1% O_2 and stained for the indicated proteins. **(B)** Western blot of SF3B1,
795 HIF1α and GAPDH of PANC-1 cells exposed to 21% or 1% O_2 for 12 hours. **(C)** Transfection of a wildtype (WT)
796 or HRE-mutated *SF3B1* promoter-luciferase reporter (mutHRE = AAAAA) together with either an empty vector
797 control, or HIF1αΔΔP in SK-MEL28 cells. Data are shown as mean ± S.D. of biological replicates (n=3). **
798 P<0.01 normalized to mock wtHRE, two-tailed unpaired t-test. **(D)** Relative SF3B1expression in the indicated
799 patient-derived organoids and cell lines, engineered with CRISPR-Cas9 (mono-allelic loss of *SF3B1*) or treated
800 with siRNA, and measured by qPCR. In PANC-1 cells two different guide RNAs were used to target *SF3B1*. Data
801 are shown as mean ± S.D. of biological replicates (n = 3). The data is normalized to the respective unedited cell
802 line (CRISPR-Hetloss) or treatment with control siRNA. Expression levels are relative to *TBP*. **(E)** Western blot
803 analysis for FLAG in protein extracts from PANC-1 cells overexpressing FLAG-tagged SF3B1 **(F)** Transfection
804 of a *VEGF* promoter-luciferase reporter alone or together with either HIF1αΔΔP (the constitutively active form
805 of HIF1α), or in combination with different concentrations of SF3B1 plasmid in AsPC-1 cells. **(G)** VEGF
806 promoter-luciferase reporter activity in PANC-1 cells treated with control siRNA or *SF3B1*-targeting siRNA
807 (siSF3B1) cultured in hypoxia for 24 hours and exposed to the indicated doses of PX-478 (n=4). **(H)** Intron
808 retention assessed by qPCR; expression levels are relative to the housekeeping gene *TBP*. Data are shown as mean
809 ± S.D. of biological replicates (n ≥ 3). One-way ANOVA followed by a Dunnet's multiple comparison post-test.
810 **(I and J)** Protein extracts from HEK293T cells treated with siRNA targeting SF3B1 (G) or HIF1α (H), exposed
811 to 21% or 1% O_2 for 12 hours and processed for immunoblotting for the indicated proteins. **(K)** PANC-1 cells
812 were transfected with HA-tagged HIF1α and cultured in hypoxia. Lysates were then processed for
813 immunoprecipitation with an anti-HA antibody (HA-IP) followed by immunoblotting for the indicated proteins.

814

Supplementary Figure 2

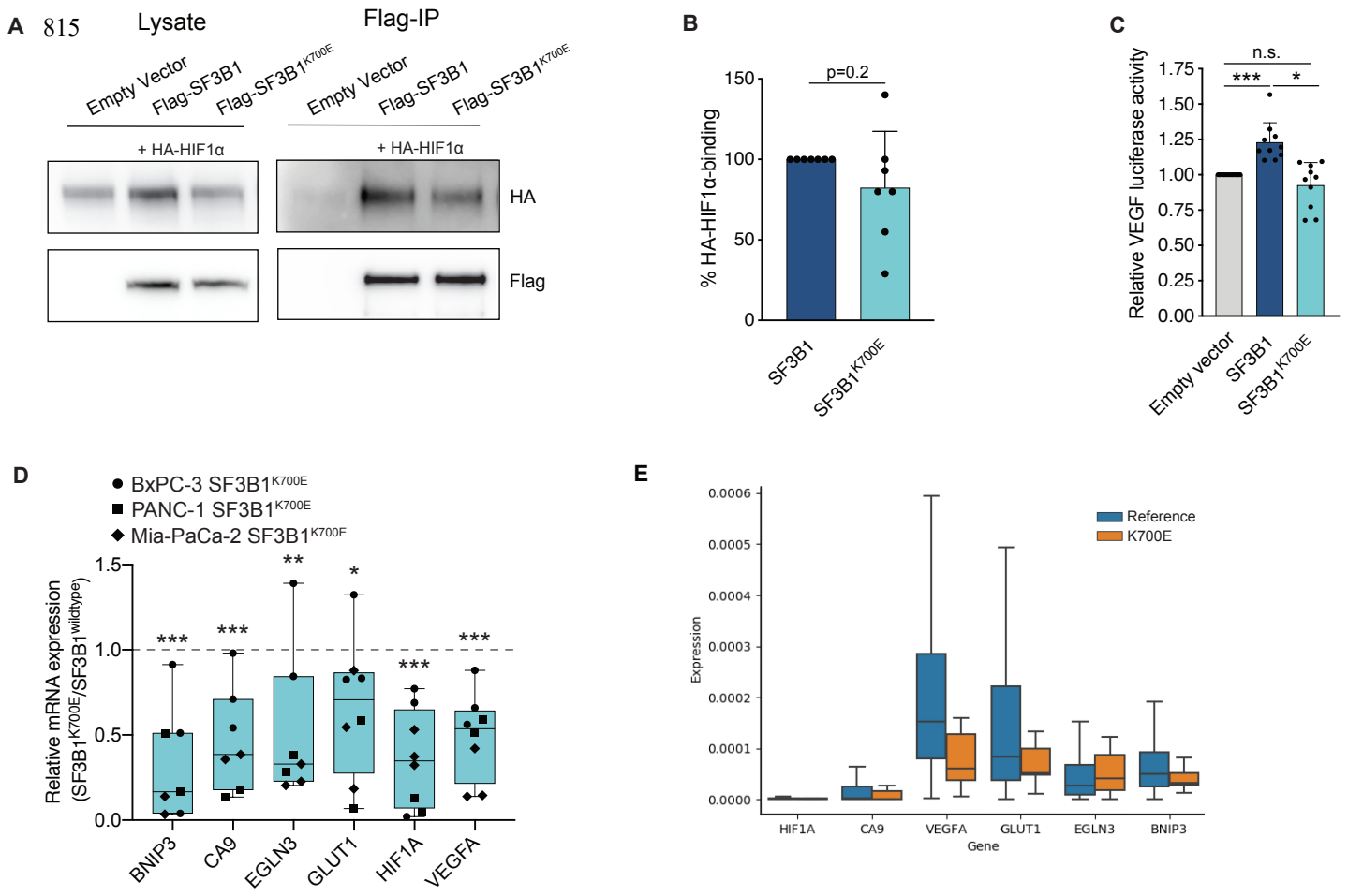

816 **Supplementary Figure 2. SF3B1-K700E mutation does not increase HIF1-response. (A)** Representative
817 Western-blot of the Co-IP of HA-tagged HIF1α and FLAG-tagged wildtype SF3B1, and its variant K700E. **(B)**
818 Quantification of HA-tagged HIF1α in HEK293T cells, pulled down with the indicated SF3B1 variants. The
819 data are represented as mean ± S.D. of independent experiments (n = 7). P-value was calculated by a two-tailed
820 unpaired t-test. **(C)** Transfection of the indicated constructs in HEK293T cells stably expressing a HIF-
821 luciferase reporter. Data are shown as mean ± S.D. of biological replicates, indicated by data points. *<P0.05,
822 **P<0.01, ***P<0.001, two-tailed unpaired t-test. Data are normalized to transfection of an empty vector
823 construct. **(D)** qPCR analysis of HIF-target genes in the indicated cell lines overexpressing *SF3B1*^{K700E} after
824 exposure to 1% O_2 for 8 hours. Data are normalized to the respective cell lines overexpressing wildtype *SF3B1*
825 after exposure to 1% O_2 for 8 hours. Expression levels are relative to the housekeeping gene *TBP* (n = 2-3).
826 Each data point represents an individual experiment of the depicted cell line. * P<0.05, ** P<0.01, *** P<0.001,
827 two-tailed unpaired t-test. **(E)** Pan-cancer analysis of selected HIF-target genes in patient samples with
828 *SF3B1*^{K700E} (orange) or *SF3B1* (blue). Only solid cancers in the TCGA database were used for analysis
829 (reference = 8243 samples; *SF3B1* = 12 samples).

Supplementary Figure 3

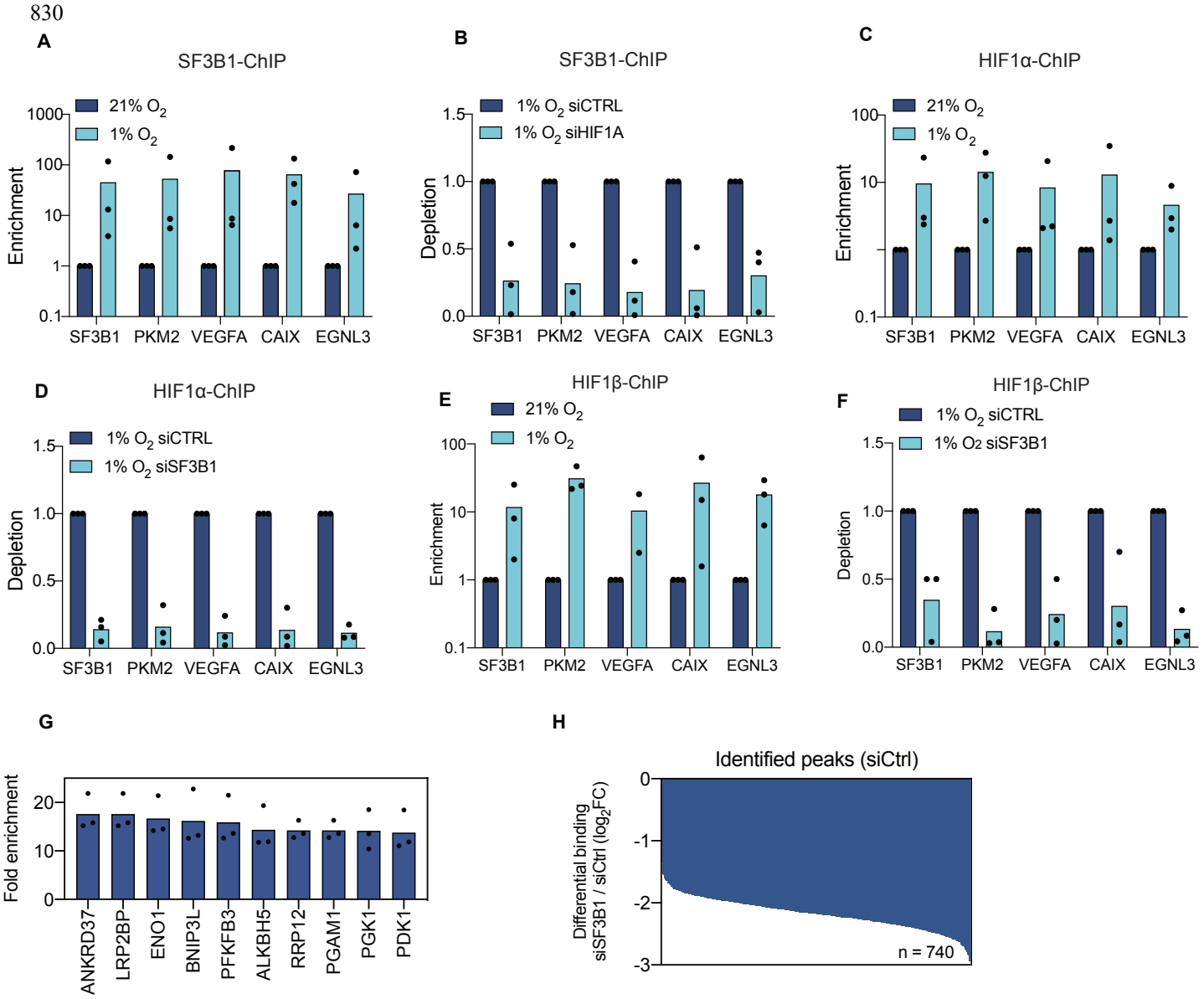

831 **Supplementary Figure 3. SF3B1 increases binding of HIF1α to its target genes. (A to F)** Chromatin
832 immunoprecipitation (ChIP) using a specific antibody against SF3B1 (A, B) HIF1α (C, D) or HIF1b (E, F) in
833 HEK293T cells. (A, C, E): Cells are cultured under 21% or 1% O_2 for 8 hours. The fold-increase in target gene
834 binding under hypoxia is shown relative to normoxia. (B, D, F): Cells are transfected with siRNA targeting
835 HIF1α (B), SF3B1 (D, F) or scrambled siRNA as control, and incubated in 1% O_2 for 8 hours. The decrease in
836 target gene binding in siRNA treated cells is shown relative to the siRNA control. Results show three
837 independent experiments. **(G)** Fold enrichment over input of the 10 highest enriched peaks of the siCtrl-treated
838 samples identified by HIF1α-ChIP-Seq. **(H)** Differential binding analysis of peaks shown in Fig. 3D in PANC-1
839 cells treated with siSF3B1 compared to siCtrl, identified by HIF1α-ChIP-Seq.

Supplementary Figure 4

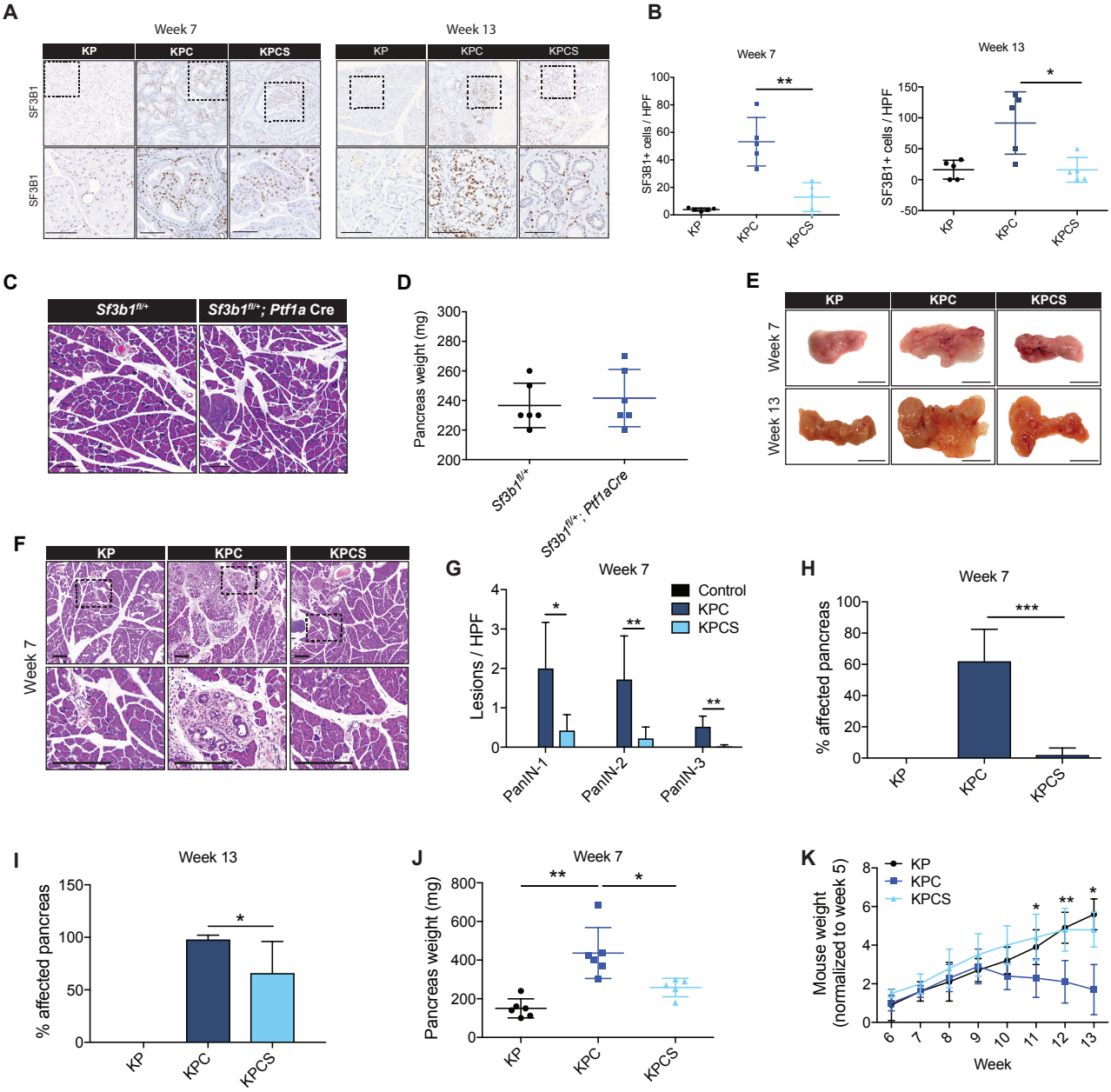

840 **Supplementary Figure 4. Effect of SF3B1 reduction on PDAC growth. (A)** Representative
841 immunohistochemical staining for SF3B1 in pancreata from 7- and 13-week-old KP, KPC and KPCS mice.
842 Dashed lines indicate the area magnified below. Scale bar is 100 µm. **(B)** Quantification of SF3B1 positive areas
843 in KP, KPC and KPCS mice at 7 and 13 weeks of age. Ten high power fields (HPF) were analysed per animal (n
844 = 5). * P<0.05. One-way ANOVA followed by a Tukey's multiple comparison post-test. **(C)** H&E staining of
845 pancreata from *Sf3b1*$^{fl/+}$ and *Sf3b1*$^{fl/+}$*; Ptf1aCre* mice at 13 weeks of age. Representative images, scale bar is 100
846 µM. **(D)** Evaluation of pancreas weight of *Sf3b1*$^{fl/+}$ and *Sf3b1*$^{fl/+}$*; Ptf1aCre*, mice at 13 weeks of age. The data are
847 represented as mean ± S.D. (n = 6-7). **(E)** Representative photographs of KP, KPC, and KPCS pancreata from 13
848 weeks-old mice. Scale bar: 1cm. **(F)** Representative images of H&E staining revealing the histopathologic lesions
849 in pancreata of KP, KPC and KPCS mice at the indicated age. Square dashed lines indicate the area magnified in
850 the image below. Scale bar is 100 µm. **(G – I)** Quantification of the prevalence of mPanIN and PDAC in the
851 H&E-stained pancreatic sections of 7-week-old KP, KPC and KPCS mice (G). Quantification of the affected
852 pancreas at the indicated age (H, I). Ten high power fields (HPF) were analysed per animal. The data are
853 represented as mean ± S.D. (n = 5). * P<0.05, ** P<0.01, *** P<0.001. One-way ANOVA followed by a Tukey's
854 multiple comparison post-test. **(J)** Pancreas weight of KP, KPC and KPCS mice at 7 weeks of age. The data are
855 represented as mean ± S.D. (n = 6-7). * P<0.05, ** P<0.01, *** P<0.001. One-way ANOVA followed by a
856 Tukey's multiple comparison post-test. **(K)** Body weight of KP, KPC, and KPCS mice at indicated time point
857 over a period of 13 weeks. The data are normalized to body weight of the mice at 5 weeks of age and represented
858 as mean ± S.D. (n = 6-8). * P<0.05, ** P<0.01. One-way ANOVA followed by a Tukey's multiple comparison
859 post-test.

Supplementary Figure 5

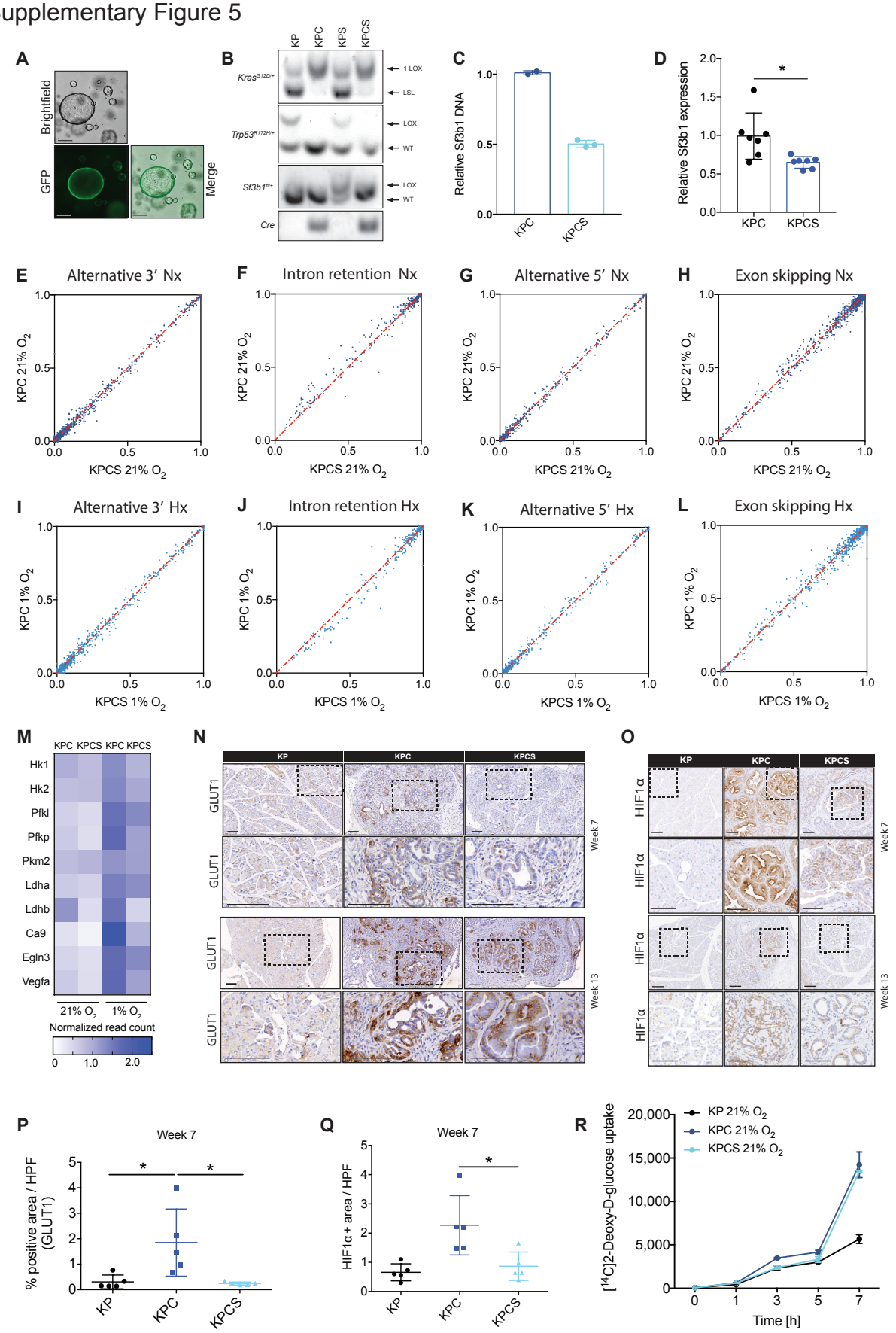

860 **Supplementary Figure 5. *Sf3b1* heterozygosity affects PDAC growth via HIF signalling. (A)** Bright field and
861 fluorescence images of mouse organoids transduced with a GFP-Cre virus after FACS. **(B)** Representative PCR
862 analysis of genomic DNA from KP, KPC, KPS and KPCS organoids. The Cre-mediated recombination of the
863 conditional allele *KrasG12D/+*, *Trp53R172H/+* generates a single LoxP site and 2 LoxP sites for *Sf3b1*. (**C**) *Sf3b1*
864 DNA levels at exon 5 for validation of monoallelic Sf3b1 knockout in the indicated organoid lines assessed by
865 qPCR. Values were normalized to *Sf3b1* exon 2 DNA levels, which remain unaffected by Cre-lox recombination.
866 **(D)** *Sf3b1* mRNA expression of KPC and KPCS organoid lines. *P<0.05, ** P<0.01, two-tailed unpaired t-test.
867 **(E-L)** Scatter plot of alternative 3' end usage (E, I), intron retention (F, J), alternative 5' end usage (G, K) and
868 exon skipping (H, L) events in KPC and KPCS organoids cultured in normoxia (E to H) and hypoxia (I to L).
869 Events were computed by SplAdder(Kahles et al., 2016), only high confidence events were considered for the
870 analyses. **(M)** Heatmap displaying normalized read counts for the indicated genes derived by RNA-sequencing.
871 **(N)** Representative immunohistochemical staining for GLUT1 in pancreata from 7-week and 13-week old KP,
872 KPC and KPCS mice. Dashed lines indicate the area magnified below. Scale bar: 100 µm. **(O)** Representative
873 immunohistochemical staining for HIF1α in pancreata from 7-week and 13-week old KP, KPC and KPCS mice.
874 Dashed lines indicate the area magnified below. Scale bar: 100 µm. **(P)** Quantification of GLUT1 positive areas
875 in KP, KPC and KPCS mice at 7 weeks of age. Ten high power fields (HPF) were analysed per animal (n = 5). *
876 P<0.05. One-way ANOVA followed by a Tukey's multiple comparison post-test. **(Q)** Quantification of HIF1α
877 positive areas in KP, KPC and KPCS mice at 7 weeks of age. Ten high power fields (HPF) were analysed per
878 animal (n = 5). * P<0.05. One-way ANOVA followed by a Tukey's multiple comparison post-test. **(R)** KPC and
879 KPCS organoids were incubated in normoxic conditions in medium containing [^{14}C]-2-deoxyglucose at different
880 time-points and processed for glucose uptake measurements. Counts were normalized to the cell number (*n* = 4
881 biological replicates per time point and condition). ** P<0.01, One-way ANOVA followed by a Tukey's multiple
882 comparison post-test.

Supplementary Figure 6

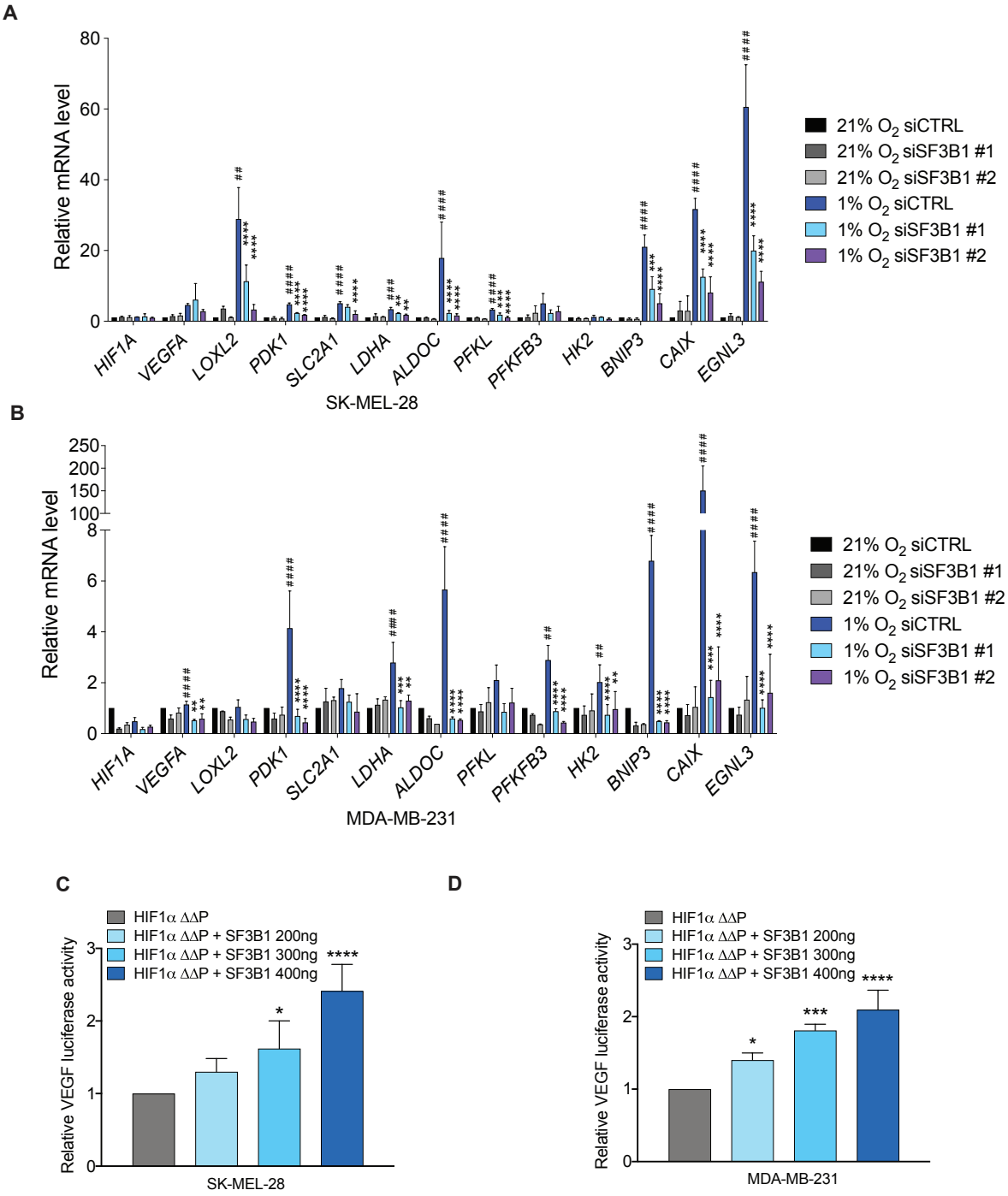

883 **Supplementary Figure 6. SF3B1 reduction affects HIF signalling in cancer cell lines. (A and B)** qPCR
884 analyses of the indicated genes in SK-MEL-28 (A) and MDA-MB-231 (B), transfected with the depicted siRNAs
885 and incubated in 21% or 1% O_2 for 12 hours. Expression levels are relative to *TBP*. Data are shown as mean ±
886 S.D. of biological replicates (n=3). *P<0.05, **P<0.01, ****P<0.0001, data normalized to 1% O_2 siCTRL. For #
887 P<0.05, ## P<0.01, #### P<0.0001, data are normalized to 21% O_2 siCTRL. Two-tailed unpaired t-test. **(C and**
888 **D)** Transfection of a *VEGF* promoter-luciferase reporter alone or together with either HIF1αΔΔP (the
889 constitutively active form of HIF1α), or in combination with different concentrations of SF3B1 plasmid in SK-
890 MEL-28 (C) and MDA-MB-231 cells (D). Data are shown as mean ± S.D. of biological replicates (n = 3).
891 *<P0.05, **P<0.01, ***P<0.001, **** P<0.0001. One-way ANOVA followed by a Dunnet's multiple
892 comparison post-test.

Supplementary Figure 7

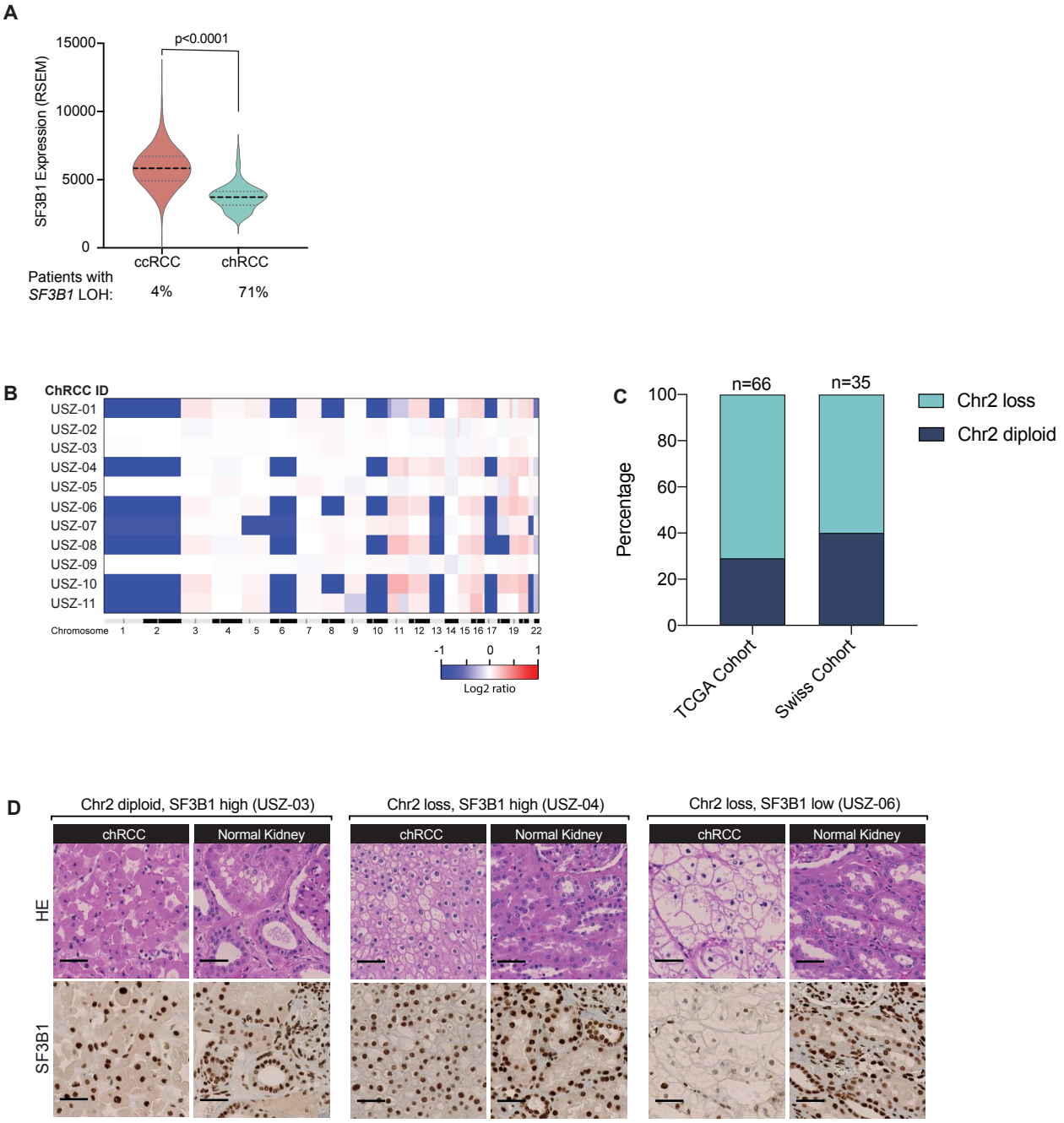

893 **Supplementary Figure 7. *SF3B1* heterozygosity is frequently observed in chRCC. (A)** Expression of SF3B1
894 and loss of heterozygosity (LOH) in clear cell renal cell carcinoma (ccRCC) and chromophobe renal cell
895 carcinoma (chRCC) based on TCGA data. One-way ANOVA followed by a Tukey's multiple comparison post-
896 test. **(B**) Copy number variations (CNV) analysed with array-based comparative genome hybridization (array-
897 CGH) of tumors from 11 chRCC patients of the Swiss-cohort. **(C)** Chromosome 2 status in chRCC samples of
898 the TCGA cohort and the Swiss cohort. The Swiss cohort is composed of samples published by Ohashi et al.,
899 2019 (n=24) and the samples shown in Suppl. Fig. 5A (n=11). **(D)** Representative H&E and IHC staining of
900 SF3B1 chRCC patients without loss (left) and with loss (middle and right) of chromosome 2. The middle staining
901 shows compensation of heterozygous loss of *SF3B1*, whereas the sample on the right has reduced levels of SF3B1.
902 Scale bar is 50µm.